Design of an X-ray diffractometer (XRD) for a Mars-rover

Melenhorst, R.W.J.

Award date:
2006

Design of an X-ray diffractometer (XRD) for a Mars-rover

Master's thesis

R.W.J. Melenhorst

DCT 2006.14

Supervisor:	Prof.dr. H.Nijmeijer	
Coaches:	Dr.ir. P.C.J.N. Rosielle	
	Drs. A.A. Wielders	Space Horizon, Haarlem
	Ir. J.A.C.M. Pijnenburg	TNO Science & Industry, Delft
	Dr.ir. R. Delhez	TU Delft, Delft

Technische Universiteit Eindhoven
Department of Mechanical Engineering
Dynamics and Control Technology, Constructions & Mechanisms

Eindhoven, 6th February 2006

Summary

ExoMars is a space program of the European Space Agency (ESA). Its aim is to characterise the biological environment on Mars in preparation for robotic missions and then human exploration. The mission will make use of a Mars orbiter, a descent module and a Mars rover. An X-ray diffractometer is proposed as payload on the Mars-rover. The assignment of this master thesis was to design an X-ray diffractometer that can meet the requirements dictated by ESA for extraterrestrial missions and meet the X-ray diffraction requirements.

The design is based on two levers which rotate a radioactive source and a solid state detector around a mutual axis. This axis coincides with the surface of the specimen to be analysed. The two levers will rotate in a stacked, integrated, hybrid bearing set. To avoid play all mating surfaces have a tight fit. The angular contact ball bearings are preloaded by one spring bush to save mass and volume. In order to realise this, the outer shaft has an axial degree of freedom. The levers consist of a double leaf spring, constraining all degrees of freedom except one. This degree of freedom and the rotation around the axis are constrained by a piezo stepper which 'walks' along a guide. The step resolution is 15μrad but can be increased. Two optical angle encoders provide the angle information of the levers. A launch-lock shall keep the levers in place during launch and impact on Mars. The diffractometer components are enclosed by two shells, providing stiffness, vacuum environment and protection. A beryllium window provides passage for the X-rays.

The design almost completely meets its requirements. All components are vacuum compatible and meet the requirements for space qualification. Tests should give more information about the performance and the maximal resolution of the stepper.

Samenvatting

ExoMars is een ruimtevaart-programma van de European Space Agency (ESA). Het doel van het programma is het beschrijven van de biologische omgeving op Mars in voorbereiding op robot- en uiteindelijk bemande missies. De Exomars-missie maakt gebruik van een Mars-satelliet, een landingsmodule en een Mars-rover. Een röntgendiffractometer is voorgesteld als onderdeel van de rover lading. De opdracht van dit afstudeerproject was het ontwerp van een röntgendiffractometer dat voldoet aan ESA's eisen voor buitenaardse missies en aan eisen met betrekking tot röntgendiffractie.

Het ontwerp is gebaseerd op twee armen die een radioactieve bron en een röntgendetector roteren om een gemeenschappelijke as. Deze as valt samen met het oppervlak van het te analyseren preparaat. De twee armen roteren in een gestapelde, geïntegreerde en hybride lageropstelling. Om speling te vermijden zijn alleen vaste passingen toegepast. Om massa en volume te beperken, worden twee sets hoekcontactlagers voorgespannen door middel van één harmonicabus. Hiervoor is één as uitgevoerd met een axiale vrijheidsgraad. De armen bestaan uit een dubbele bladveer. De hierdoor vrijgelaten vrijheidsgraad in axiale richting en de positie van de as worden vastgelegd door een piëzo-stepper. Deze piëzo-stepper "loopt" langs een geleiding en bepaald de positie van de röntgenbron en detector. De stapresolutie is 15 μrad maar kan nog verder verlaagd worden. Twee optische encoders geven de positie van de armen weer. Een lanceeerbeveiliging moet de armen op de plaats houden tijdens lancering en bij het neerkomen op Mars. De onderdelen van de diffractometer worden ingesloten door twee schalen, welke voorzien in stijfheid, een vacuumomgeving en bescherming. Een beryllium venster zorgt voor vrije doorgang van de röntgenstralen.

Het ontwerp voldoet bijna geheel aan de gestelde eisen. Alle onderdelen zijn geschikt voor een vacuumomgeving en voldoen aan de eisen voor space qualification. Testen moeten meer inzicht geven in de prestaties en de maximale resolutie van de piëzostepper.

Preface

This report describes the results of my graduation project at the Constructions and Mechanisms group of the Technische Universiteit Eindhoven. The project is carried out under authority of the precision mechanics department of TNO Science and Industry in Delft.

During my assignment I received a lot of help and support by many people. Herewith I would like to show my gratitude.
In the first place I would like to thank my coaches, Nick Rosielle, Arno Wielders, Joep Pijnenburg and Rob Delhez for their time, help and advise.
In the second place, but invaluable, the people at the precision engineering department of TNO, the students at the Constructions and Mechanisms lab, friends and family.

Contents

Symbols and definitions

List of symbols

a	acceleration	m/s^2
c	stiffness	N/m
C_0	static load rating	N
C	capacitance	F
d	interplanar spacing	m
E	Young's modulus	N/m^2
E′	effective modulus of elasticity	N/m^2
f	frequency	Hz
f_e	eigenfrequency	Hz
F	force	N
F_f	friction force	N
F_N	normal force	N
F_t	tangential force	N
F_1	maximal contact load	N
g	earthly acceleration (9.81)	m/s^2
G	Shear modulus of elasticity	N/m^2
G_{RMS}	Root mean square acceleration	m/s^2
h_m	stroke	m
i	transmission ratio	-
m	mass	kg
p_c	critical mean pressure	N/m^2
P	power	W
P	bearing load	N
r	radius	m
r_s	distance specimen-source	m
r_d	distance specimen-detector/receiving slit	m
r_θ	rotation around the θ-axis	-
r_r	rotation around the r-axis	-
r_z	rotation around the z-axis	-
R′	effective radius	m
R_r	race conformity	-
$R_{p0,2}$	yield strength	N/m^2
S	circumference	m

t	time	s
t_d	detection time	s
t_m	moving time	s
T	temperature	K
tanδ	dielectric factor	-
u	movement	m
U	voltage	V
v	velocity	m/s
x	position	m
z	position	m
z	number of bearing balls	-
α	coefficient of thermal expansion	1/K
β	angle of divergence	$^\circ$
δ	indentation	m
ε	peak to peak distance	m
φ	angle	rad
λ	wavelength	m
μ	friction coefficient	-
ν	Poisson's ratio	-
θ_d	angle incident beam-specimen	rad
θ_s	angle diffracted beam-specimen	rad
ρ	density	kg/m^3
σ	stress	N/m^2
ξ	damping factor	-

Coordinate system

The coordinate system used is a cylindrical coordinate system r-θ-z with its origin on the specimen surface. Rotations about the r, θ and z-axis are respectively r_r, r_θ and r_z.

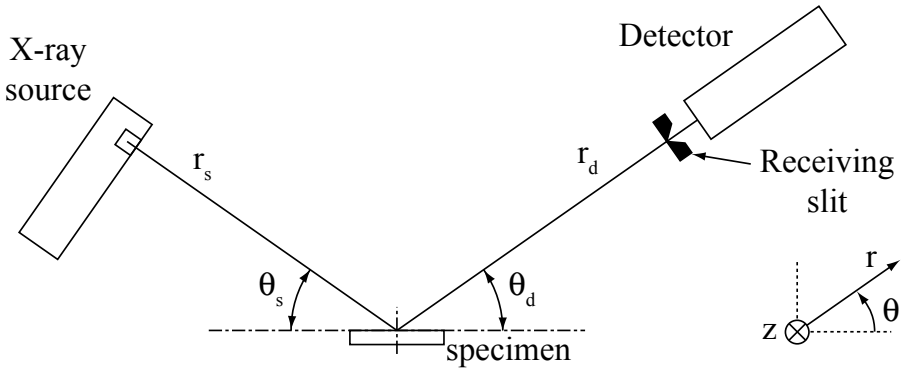

Figure 1: Axes definition

Chapter 1

Introduction

The Aurora programme is set up by the European Space Agency (ESA) with the primary objective to create, and then implement, an European long-term plan for the robotic and human exploration of the solar system, with Mars, the moon and the asteroids as the most likely targets [12]. For the Aurora programme ESA adopts a step by step approach whereby the complexity of the missions will increase in time. If all goes well the ultimate goal will be a human expedition to Mars by the year 2030. One of the first missions to Mars will be the ExoMars mission.

The aim of the ExoMars mission is to characterise the biological environment on Mars in preparation for robotic missions and then human exploration. The mission will make use of a Mars orbiter, a descent module and a Mars rover [12]. The rover will be equipped with a 40 kg exobiology instrument payload (Pasteur package) which includes a lightweight drilling system, a sampling and handling device and other instruments to search for signs of past or present life. Using conventional solar arrays to generate electricity, the rover will be able to travel autonomously a few kilometres on the Mars surface while gathering scientific information. Figure 1.1 gives an impression of the Mars rover.

Figure 1.1: Artist impression of a Mars rover [11]

In response to a 'call for ideas' issued by ESA, an international team (Mars-XRD team) proposed an X-ray diffractometer as part of the surface exploration payload of the Pasteur package. This team consists of companies, universities and institutes from various European countries, including the Netherlands Organisation for Applied Scientific Research TNO (TNO) and Delft University of Technology.
X-ray diffraction (XRD) is the only analysis method to get detailed insight in the mineralogy and chemical composition of the Mars soil and may solve questions about (i) the geology and mineralogy of Mars, (ii) the whereabouts of large amounts of water and carbon dioxide that are remnants of the much larger amounts of liquid water and carbon dioxide gas on Mars of about three billion years ago,(iii) an indication for the presence of present or past life on Mars [8].
Apart from an X-ray fluorescence (XRF) device on the Viking Lander no diffractometers have been sent into space yet but currently also NASA is working on this topic [23].

TNO (see Appendix I) has a wide experience in designing space instruments, however the design of an X-ray diffractometer is completely new. Therefore, parallel to the Mars-XRD project this MSc-graduation project has been started by TNO and Delft University of Technology in order to provide a proof of concept which can serve as knowledge acquisition and as possible reference and/or backup to the Mars-XRD team. Possibly a trade-off can be made for terrestrial application in the form of a portable diffractometer. This report describes the design of the XRD for the Pasteur package.

In the next chapter objectives and assignment are explained. Chapter 3 provides a concise theoretical background on X-ray diffraction. In chapter 4 the requirements will be elaborated. Chapter 5 and 6 explain the diffractometer design and the choices made for this design. Chapter 7 gives an evaluation of the diffractometer design and finally in chapter 8 conclusions and recommendations are given.

Chapter 2

Objectives and Assignment

2.1 Objectives

The objective of this assignment follows from the desire to bring an X-ray diffractometer to Mars in order to characterise its biological environment.

The main objective is to present a design of an X-ray diffractometer that can meet the requirements dictated by ESA for extraterrestrial missions and meet the X-ray diffraction requirements.

A second objective is knowledge acquisition. For TNO (even if the design will not be used as payload) this assignment will provide knowledge and experience in the design of a small size diffractometer and a possible trade off to a commercial portable diffractometer can be made.

2.2 Assignment

The assignment has been described as follows:

> Design an X-ray diffractometer that can meet the requirements dictated by the diffraction process, space- and planetary protection policy and by ESA.

The assignment comprises the following items:

- Review of requirements
- Conceptual design
- Detailed design of main components

Chapter 3

X-ray powder diffraction

This chapter will give a basic understanding of X-ray diffraction and the diffractometer. It addresses the interaction between radiation and matter, powder diffraction and the diffractometer. The chapter is only a short introduction to X-ray powder diffraction. Minor effects originating from the X-ray−matter interaction are not taken into consideration. The process will be treated as 2D process though actually it is a 3D process. More detailed information can for instance be found in [20].

3.1 X-ray Diffraction

3.1.1 Atom-radiation interaction

X-rays are part of the electromagnetic spectrum and therefore have properties of both waves and particles. The packets of energy (photons) can 'bounce' and transfer momentum, which is a property of a discrete particle. They can also be diffracted by a grating of appropriate wavelength and have measurable wavelengths, which are properties of a wave. When X-rays interact with matter there is a distinction between processes where the wavelength changes (mainly the photoelectric effect) and a process where the wavelength remains the same.

With the photoelectric effect an incoming photon dislodges a K-shell electron in the target atom, leaving a vacancy in that shell. An outer shell electron then 'jumps' to fill the vacancy. This results in the generation of a characteristic X-ray photon with an energy equivalent to the energy of the jump. The process is called fluorescence.

The second process is the one important for X-ray diffraction. The wave properties of X-rays involve a periodical change of electrical and magnetic field. With electrically loaded particles an interaction is to be expected: electrons will oscillate in phase with an X-ray beam and will become themselves X-ray point sources of the same wavelength. This effect is called scattering. There is no interaction with the nucleus because of its high mass. The interaction of an atom and an X-ray beam will result in scattering by the atom which is essentially the sum of the scattering of the electron 'cloud' around the nucleus. When the atoms are arranged in a regular structure (i.e. crystalline) the X-rays scattered by the individual atoms will interfere. Most rays will be out of phase and cancel out each other (destructive interference) but in specific directions the rays will be in phase and will amplify each other (constructive interference). This process of constructive interference is called diffraction.

3.1.2 Diffraction

As mentioned in the previous section diffraction is based on the scattering of regular arranged atoms. L. Bragg and his father W.H. Bragg discovered that diffraction could be treated as a reflection from evenly spaced planes of atoms if monochromatic x-radiation was used. 'Reflection' of X-rays differs from reflection of visible light in that visible light is reflected at all angles, whereas X-rays only 'reflect' at specific angles.

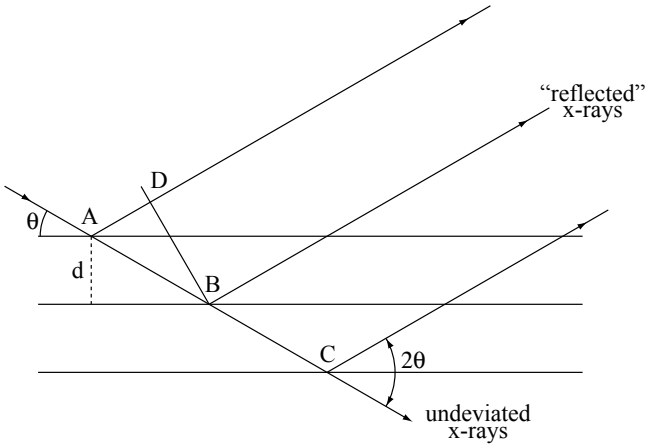

Figure 3.1: Condition for X-ray reflection

The condition for 'reflection' is depicted in figure 3.1. An incident beam with wavelength λ, penetrates a stack of planes of spacing d. The angle of incidence is called θ. Each plane will 'reflect' a portion of the incident beam. Constructive interference will occur if the 'reflected' beams are in phase, that is, if the path difference AB-AD=nλ, where n is an integer. This condition is fulfilled when:

$$2dsin(\theta) = n\lambda \tag{3.1}$$

This equation is called Bragg's law. Herein n is called the order of diffraction.

3.1.3 X-ray powder diffraction

The Bragg law makes X-ray powder diffraction analysis possible. X-ray powder diffraction is used for both qualitative and quantitative analysis of a specimen. In X-ray powder diffraction, a powder irradiated at a given angle of incidence θ will produce a diffraction pattern. In this case powder does not automatically means small loose particles. Important are the number and size of the individual crystallites. In this way both a polycrystalline solid as well as billions of tiny crystallites can be considered to be powder. For the X-rays to yield useful information about the material structure, the wavelength of the incident X-rays should be of that same order of magnitude as the interatomic spacing in the crystal structure.
A typical diffraction pattern consists of a plot of diffracted intensities versus the diffraction angle, see figure 3.2. By convention diffraction angles are recorded as 2θ (the angle between the directions of the incident and 'reflected' rays, see fig 3.1).

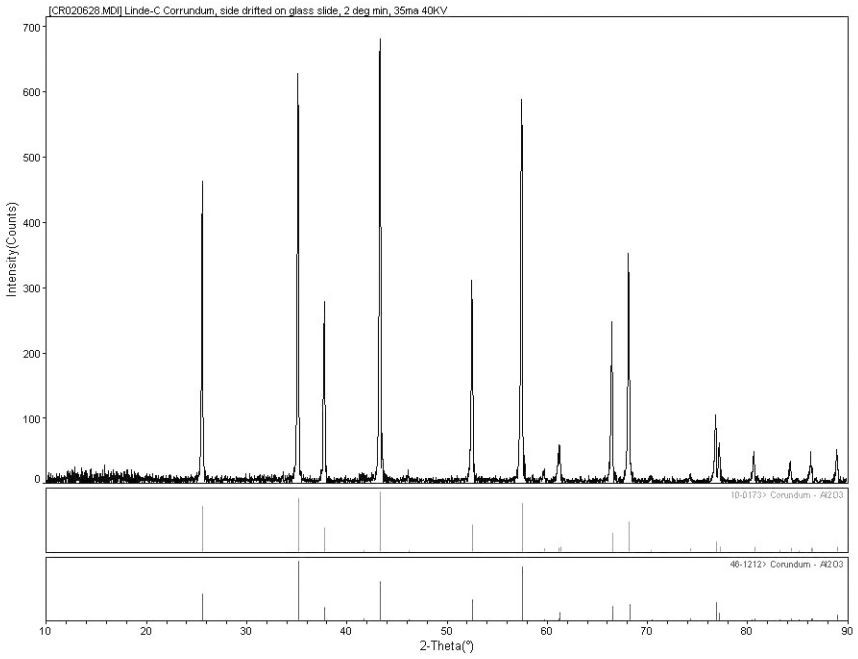

Figure 3.2: Typical diffraction pattern

The three parameters of special interest in a diffraction pattern are:

- The position of the diffraction lines

- The intensities of a diffraction line

- The intensity distribution within a diffraction line as a function of diffraction angle

The positions of the diffraction lines are used to determine the unit cell dimensions of the target material. The intensities and the distribution of the diffracted X-rays can be used to work out the kind and arrangement of atoms in a unit cell. Qualitative analysis, also called phase analysis, usually involves the comparison of diffraction patterns with known measured or calculated patterns. The International Center Diffraction Data (ICDD) provides a database with these patterns.

3.2 The X-ray powder diffractometer

Figure 3.3 shows the essential parts of an X-ray diffractometer. A powder specimen C is irradiated by a divergent X-ray beam from the X-ray source S. Rays diffracted by the specimen form a convergent beam which comes to focus at the receiving slit RS and then enters the detector D. A and B are special slits which limit and collimate the incident and diffracted beams. The main components are shortly discussed in the next paragraphs.

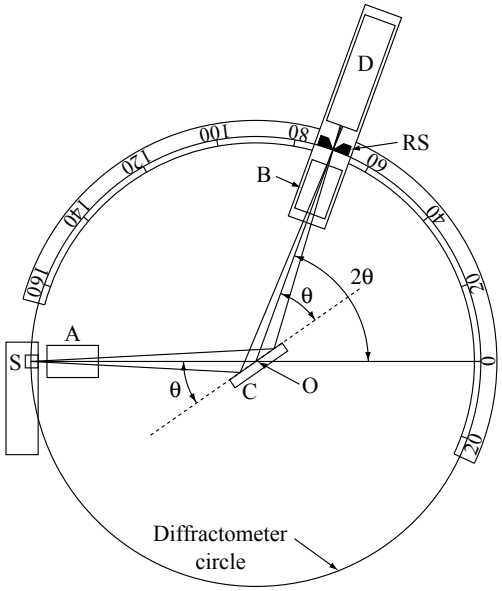

Figure 3.3: X-ray diffractometer components

X-ray source

Most diffractometers use an X-ray tube as source. When accelerated electrons in the tube strike the target material, X-radiation is emitted. The tube source acts as a line source. The emitted X-rays includes a continuous spectrum and the characteristic ($K_{\alpha_{1,2}}, K_{\beta}$) radiations. For X-ray diffraction only K_{α} radiation is desired.

X-ray detector

Different types of X-ray detectors can be used. Currently three types are in use: proportional, scintillation and semiconductor. All depend on the power of X-rays to ionise atoms, whether they are atoms of a gas (gas filled detectors) or atoms of a solid (solid state detectors). In general three aspects of the detector are of concern: losses, efficiency, and energy resolution. A general treatment of these detectors is given by [21].

Specimen

The specimen is a flat specimen with a surface area depending on the length of the X-ray source and the divergence of the emitted rays. Typically the surface area is 10x10 mm.

Ideally the specimen consists of a statistically infinite amount of randomly oriented powder with crystallite size less than 10 μm. It is important to avoid preferred orientation of the crystallites when mounting the specimen in the specimen holder.

Slits and filters

To limit and direct the X-rays emitted by the tube, usually slits are used. A filter is applied to monochromatise the beam, i.e. to eliminate most of the K_β radiation and to reduce the continuous spectrum. This filter can be placed in the incident or diffracted beam. The receiving slit defines the detection angle.

3.2.1 Diffractometer geometry

Focusing action

While diffractometers can differ in geometry, one returning aspect is the focusing action. The focusing action confines the observable intensity of the diffracted beams to a point where they can be accurately measured. The basis for the focusing condition is the geometrical theorem: All angles inscribed in a circle and based on the same arc SR are equal to one another and equal to half the angle subtended at the centre by the same arc AB (see figure 3.4a).

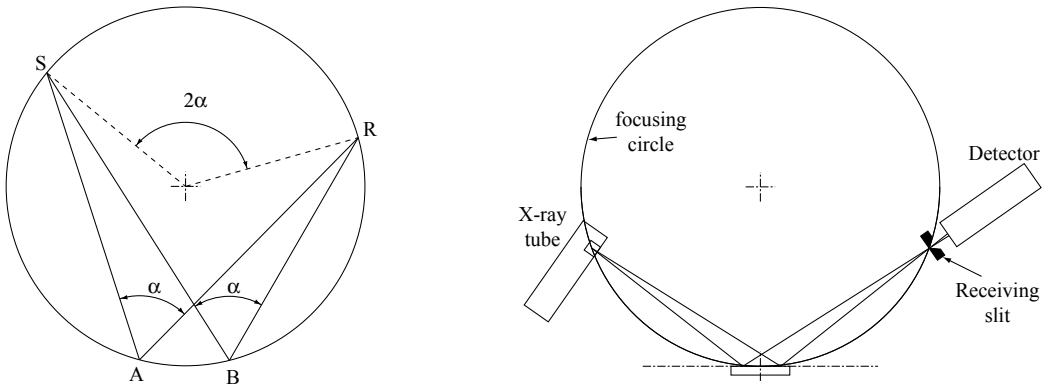

(a) (b)

Figure 3.4: Focusing geometry

In figure 3.4a S can be seen as the X-ray source and R as the receiving slit of a diffractometer (figure 3.4b). A and B are points on the specimen surface. The circle is called focusing circle. X-rays proceeding in the direction SA and SB will be 'reflected' in A and B. Since the angle of incidence equals the reflected angle, 'reflected' X-rays will come to a focus at the receiving slit R. Perfect focusing requires the specimen to be curved to fit the focusing circle. In practice most specimen are flat and the focusing is not perfect and denoted as 'parafocusing'.

Two geometries can be distinguished: Bragg-Brentano and Seeman-Bohlin geometry. Both geometries are explained by means of figure 3.5.
In this figure r_s is the distance between the X-ray source and the specimen, and r_d the distance between the specimen and receiving slit RS.

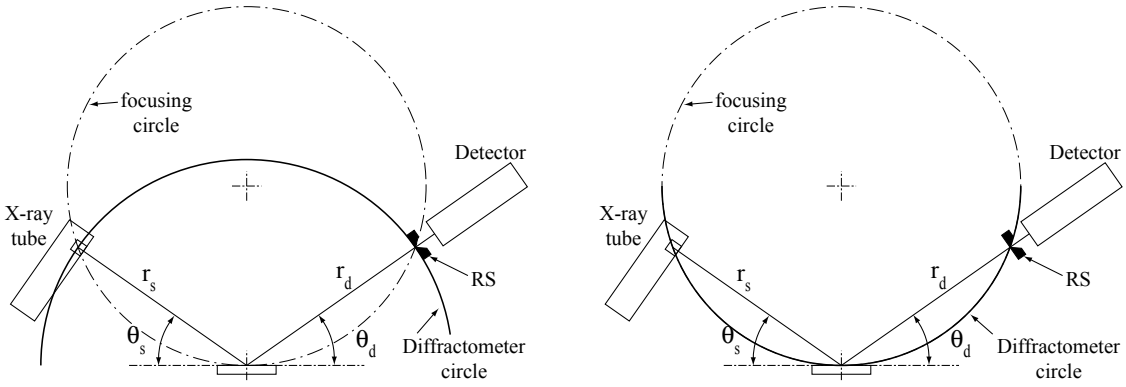

(a) (b)

Figure 3.5: Schematic diffractometer movements: (a) Bragg-Brentano geometry, (b) Seeman-Bohlin geometry

Bragg-Brentano geometry

The Bragg-Brentano geometry is the most used among diffractometers. In the diffractometer the relationship between θ (the angle between the direction of the incident beam and the specimen surface) and 2θ (the angle between the directions of incident beam and the diffracted beam) is maintained throughout the analysis. r_s and r_d are fixed and equal and define the diffractometer- or measuring circle in which the specimen is always at the centre. The geometry is called $\theta - 2\theta$ geometry if the tube is fixed and the rotation of the specimen and receiving slit are coupled in a ratio $\theta : 2\theta$. It is called $\theta - \theta$ geometry if the specimen is fixed and both the tube and receiving slit rotate at an equal angle θ. During rotation of the components the radius of the focusing circle changes.

Seeman-Bohlin geometry

The Seeman-Bohlin diffractometer can have a fixed tube and specimen. The radius r_d varies with 2θ to maintain the focusing geometry. Alternatively the source and receiving slit rotate at an equal angle θ and both r_s and r_d vary to remain on the focusing circle. During rotation of the components the radius of the focusing circle remains the same.

For accurate measurement the diffractometer components have to be aligned in such a fashion that the following conditions are satisfied:

1. line source, specimen surface, and receiving slit are all parallel,
2. the specimen surface coincides with the diffractometer axis for the Bragg-Brentano geometry or with the diffractometer circle for the Seeman-Bohlin geometry,
3. the line source and receiving slit lie on the diffractometer circle.

Chapter 4

Requirements

The requirements for the diffractometer can be divided in three sets:

- Requirements following from the diffraction process and instrument components
- Specifications given by ESA
- Requirements following from ESA's space and planetary protection policy

4.1 Requirements following from the diffraction process and instrument components

The diffraction requirements are related to the geometry chosen for the diffraction observations. The diffractometer geometry takes shape in the positions of the source, the specimen and the detector. The quality of the diffractometer is directly related to the precision of the position of these components. The position of the specimen is given. The requirements to the source and detector position are summarised in table B.1.

Angle resolution $\Delta\theta$	μrad	< 20
Angle range ($2\theta = \theta_s + \theta_d$)		$4 - 160°$
Tolerance Δr	μm	20
Tolerance Δz	μm	500
Tolerance r_r	μrad	75
Tolerance $r_{\theta-source}$	μrad	200
Tolerance $r_{\theta-detector}$	μrad	1000
Tolerance $r_{z-source}$	μrad	7.5
Tolerance $r_{z-detector}$	μrad	100

Table 4.1: Geometric tolerances

The angular resolution $\Delta\theta$ of the source/detector position defines the ability to distinguish peaks in the θ-intensity plot. This resolution is determined in Appendix B. In this appendix also the tolerances and the minimal diffraction angle are defined.

4.2 Specifications given by ESA

The diffractometer will be part of the Pasteur payload of the Mars-lander. The instruments included will all be subsystems and have to fit in the main system. Table 4.2 lists specifications that are taken from the Mars-XRD team proposal.

Dimensions	mm	220x60x120
Mass (target)	kg	0.8
Maximum power consumption	W	2

Table 4.2: ESA requirements

4.3 Requirements following from ESA's space- and planetary protection policy

For use in space the diffractometer needs to be space qualified. For operation on an extraterrestrial planet it has to comply with ESA's planetary protection policy. Since the design is intended as a proof of concept not all requirements have to be met yet but the diffractometer design will be based on these requirements.

Space qualification

Space qualification involves many issues including issues on failure risks, vacuum operation and materials used. The 'European Cooperation for Space Standardization'(ECSS) provides standards an instrument has to comply with. Appendix A gives a short overview of space qualification issues and the ECSS standards involved.
The most important quantified requirements are listed in table 4.3:

T-range	°C	-150 to +50
Eigenfrequency	Hz	>200
RMS accelerations at launch/touchdown	g	40
Vacuum condition in space	Pa	10^{-9}

Table 4.3: Space qualification requirements

Planetary protection policy

Based on the Outer Space Treaty of 1967 the Committee On Space Research (COSPAR) established some planetary protection guidelines. These guidelines impose, depending on the type of mission, requirements on spaceflight missions. The ExoMars mission is classified as a category IV mission [13].

In short the requirements imposed include a detailed documentation and a large number of implementation procedures. Important for the initial design of the diffractometer are the restricted bioload and prevention of microbial contamination including the need for sterilisation of the components. This implies:

- as low as possible use of organic materials
- as few as possible mating surfaces

4.4 Boundary conditions

The design of the diffractometer will be a conceptual mechanical design. Components such as electronics, data processing and interfaces are not considered.

Other boundary conditions:

- The XRD will make use of the mechanical structure, the power supply, the central control unit and the thermal insulation of the Pasteur package.
- The Pasteur package's operation temperature will be held above 0 °C within a range of 1°C. The operation temperature may be chosen at another value later, but this possibility is not considered in this report.
- The position of the sample will be given and fixed.
- Sample surface dimension: 10x10 mm

Chapter 5

Diffractometer system layout

Several configurations are possible for the diffractometer layout. In this chapter the options will be discussed and a system layout will be presented. The individual choices made in this chapter and the next, are based only on a diffractometer for application on a Mars-rover. A possible earthly trade-off is not considered in the design because requirements for space and earth are not always corresponding.

5.1 Selection criteria for the diffractometer basics

Mechanical selection criteria for the various (sub)concepts are, in order of importance, the (estimated):

- mass and occupied volume,
- complexity, in terms of the number of separate components, pivots and guides
- accuracy
- specimen accessibility

Criteria for the diffraction process are the:

- resolving power
- minimal measuring angle (2θ)
- maximal measuring angle (2θ)

The mechanical selection criteria rest on the requirements for space operation as described in the requirements section and appendix A. Starting point is to keep the design as simple as possible (low complexity). This means as few moving parts as possible without restraining the (diffraction) requirements. Pivots and guides will be kept to a minimum to avoid play, friction and wear. Because the handling of the specimen in the Rover is still in its pre-design stage, preferably the specimen can be accessed and handled from as many as possible directions.

5.2 Diffraction Geometry

Since the position of the specimen is given, only the detector and source move. This movement is governed by the diffraction geometry. The Seeman-Bohlin and the Bragg-Brentano geometry will be considered.

With the Seeman-Bohlin geometry the source and detector trace a path on the circumference of the focusing circle while the source stays directed at the specimen (also located on the circumference). The mechanical axes of rotation of the source and the detector can coincide with the axis of the focusing circle or with the specimen surface. In the first case an extra rotation of the source is needed to keep it directed at the specimen. Advantageous is the absence of an (virtual) axis on the specimen surface, leaving more accommodation for specimen placement. The drawback is a changing angle of the detector in respect to the diffracted X-ray beam. At low angle this will result in line broadening in the diffraction plot. In the second case the source- specimen and specimen-detector distance have to be varied.

With the Bragg-Brentano geometry the source and detector trace a path on the circumference of a circle with its axis on the specimen surface. Both source and detector are automatically directed at this axis.

5.2.1 Seeman-Bohlin versus Bragg-Brentano

Though the Bragg-Brentano geometry is most used in diffractometers, the Seeman-Bohlin can be a serious alternative. When it comes to capturing the diffraction pattern, the latter has some advantage.
With equal radius the Seeman-Bohlin geometry provides double the resolving power of the Bragg-Brentano geometry. The resolving power is defined as $\frac{d}{\Delta d}$ and is obtained by differentiating Bragg's law for n=1:

$$\begin{aligned} \lambda &= 2d\sin\theta \\ \frac{\mathrm{d}\theta}{\mathrm{d}d} &= \frac{-1}{d}\tan\theta \end{aligned} \tag{5.1}$$

thus

$$\frac{d}{\Delta d} = \frac{-1}{\Delta\theta}\tan\theta \tag{5.2}$$

The variation in angle with respect to the specimen, $\Delta\theta$, in relation to he displacement along the circumference of diffractometer circle, ΔS, differs for both geometries: $\Delta\theta = \frac{\Delta \mathrm{S}}{2\mathrm{R}}$ for the Seeman-Bohlin and $\Delta\theta = \frac{\Delta S}{R}$ for the Bragg-Brentano geometry. This is displayed in figure 5.1. For the Seeman-Bohlin geometry the resolving power is:

$$\frac{d}{\Delta d} = \frac{-2R}{\Delta S}\tan\theta \tag{5.3}$$

whereas for the Bragg-Brentano geometry:

$$\frac{d}{\Delta d} = \frac{-R}{\Delta S}\tan\theta \tag{5.4}$$

where R is the radius of the diffractometer circle.
When a square box will be taken as outline of the occupied space the volume differs for both geometries. For equal occupied space the radius of the Seeman-Bohlin geometry would be $\frac{1}{2}\sqrt{2}$ times the radius of the Bragg-Brentano geometry. In this case the difference in resolving power would be about 40%.

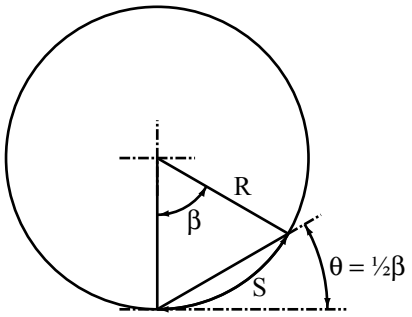

$$\left.\begin{array}{l}\Delta S = \Delta\beta R \\ \theta = \frac{1}{2}\beta\end{array}\right\} \Delta\theta = \frac{\Delta S}{2R}$$

(a)

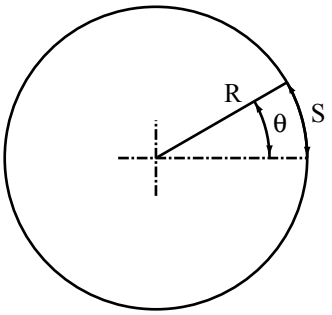

$$\Delta\theta = \frac{\Delta S}{R}$$

(b)

Figure 5.1: Resolving power: (a) Seeman-Bohlin, (b) Bragg-Brentano

The specimen surface will be about 10x10 mm. The analysed surface depends on the position of the source and the divergence of the incident beam.

In the Bragg-Brentano geometry the irradiated surface length increases with decreasing angle θ. Figure 5.2a shows an irradiated surface length larger than 10mm at angles lower than 20 °. The irradiated surface is larger than the specimen surface which means loss of intensity. Beams passing the specimen surface may cause erroneous data in the diffraction plot when diffracted by the specimen support.

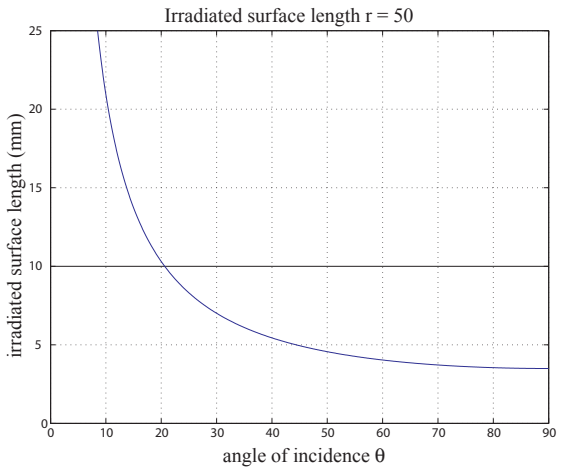

(a)

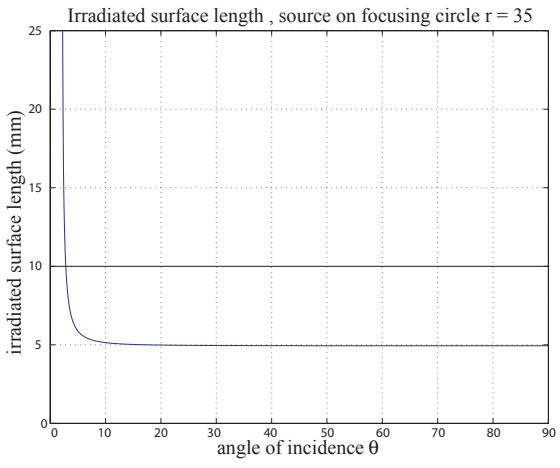

(b)

Figure 5.2: Length of irradiated surface (divergence of the incident beam 1 °): (a) Bragg-Brentano , (b) Seeman-Bohlin

The Seeman-Bohlin geometry on the other hand has an almost constant irradiated surface due to the decreasing distance between source and specimen with decreasing angle θ, see

figure 5.2b. In this figure the radius of the focusing circle is compensated as discussed in the previous paragraph. From 4° up, the specimen surface is larger then the irradiated surface which means an almost constant intensity over the whole θ range.

Though the Seeman-Bohlin has advantageous features, it has also some major drawbacks. Compared to the Bragg-Brentano geometry the Seeman-Bohlin geometry needs either an extra rotation of the source to keep the X-ray beam directed at the specimen or it needs two extra translations to keep the source and detector on the focusing circle. Apart from the added complexity and failure risk due to extra moving elements this possibly also introduces extra inaccuracy due to bearing and/or guiding tolerances.
Another drawback appears at a small diffraction angle. Both source and detector approach the specimen. Because of finite dimensions the minimal diffraction angle is restricted to the point where these elements come together. In appendix C the minimal angle is calculated: $9^\circ(2\theta)$. This angle is larger than the minimal required angle of $4^\circ(2\theta)$. Because of the smaller radius for equal volume also the maximum diffraction angle will be smaller than is the case for the Bragg-Brentano geometry. At a small diffraction angle the X-ray beams strike the detector at a small angle. Since no ideal focusing on the detector can be expected, this will lead to line-broadening in the diffraction plot.

The main advantage of the Bragg-Brentano geometry is its simple layout with a minimum of moving parts. The detector face will always be perpendicular to the X-ray beam, making the influence of deviations not θ dependent. The main drawback is the axis of rotation on the specimen surface. This can put restrictions on the accessibility for the specimen.

5.2.2 Choice of diffraction geometry

The diffractometer will make use of the Bragg-Brentano geometry. From a diffraction point of view the Seeman-Bohlin geometry has advantage. However these advantages are counterbalanced by the added complexity and the smaller angle range. The Bragg-Brentano geometry does not constrain the diffraction requirements and has a minimal amount of movements.

5.3 Miniaturisation

Commercial X-ray powder diffractometers have dimensions of about 1x1x2 meter, weight over 800 kg and can have a power consumption of 4kW. For a space flight model miniaturisation is needed.
The x-ray tube with its power supply and cooling take a great share in the total dimensions, mass and powerconsumption. By using a radioactieve source the dimensions become minimal, no power supply is needed and the mass will be in the order of several grams.
With the use of a solid state detector it is possible to keep the detector side as small as possible.
In a commercial diffractometer all data is processed inside. The space flight model only needs basic electronics to control the movements and its output can be raw data.

The diffractometer circle usually has a radius of about 200 mm. The consequences of decreasing the diffractometer circle are:

- lower mass
- less volume
- a possible higher stiffness
- a smaller minimal angle (controlled by the divergence of the beam)
- increased intensity
- a smaller maximal angle (controlled by the size of source and detector)
- a relatively (to the specimen) larger size of the source (no perfect line source)
- a lower angle resolution

The dimension requirements allow a diffractometer circle radius of about 100mm. With this radius the required angle resolution can be met while the other drawbacks (decrease of maximal angle and relative source dimension) are acceptable.

5.4 Fixed detector

With the conventional Bragg-Brentano geometry both the source and detector trace a path on the circumference of the diffractometer circle, while staying directed at the axis of this circle. Alternative paths are possible as long as the focusing condition is maintained.
An alternative of moving the detector along the circumference of a circle, is the use of a fixed detector which covers about 90 degrees of this circumference. This setup would not make use of the focusing condition and requires a parallel incident beam.
The advantages of the fixed detector are the absence of moving parts (and mass) and simple mounting. There is no need for angle measurement at the detector side and no drive is needed.However, a fixed detector has some major drawbacks.
With a focusing geometry the diffracted rays are focused, see figure 3.4 and 3.5, resulting in high measured intensities. The measured intensities without focusing are significantly lower. High resolution curved solid state detectors do not exist yet. The circumference will be approximated by linear elements. The use of these elements means a not satisfied focusing condition and the appearance of 'black spots' in the diffraction pattern where the elements join.
Current solid state detectors (e.g. CCD's) have a pixel pitch of about 15 μm. A diffractometer radius of 100mm will give an angle resolution of 150 μrad, which would not meet the requirements. This could be offset by applying a short stroke rotation of the whole detector but in that case a lot of its simplicity is lost.
The mass of a fixed detector is not necessarily lower than a moving mass because of its large support structure. When the detector has to be cooled (e.g. a CCD has to be cooled to $-40\,^{\circ}\mathrm{C}$), the whole detector area or the whole diffractometer has to be cooled. In either case this would mean a substantial increase in mass and power consumption. A moving detector only needs a small cooling element for its sensitive area though heat transfer is difficult with moving parts.

The advantages of a fixed detector are largely offset by its disadvantages. Therefore the diffractometer will make use of a moving detector.

5.5 Source and detector positioning

In order to move the source and detector along the circumference of the diffractometer circle four different mechanisms can be applied. These are depicted in Figure 5.3 and elaborated in the next paragraphs.

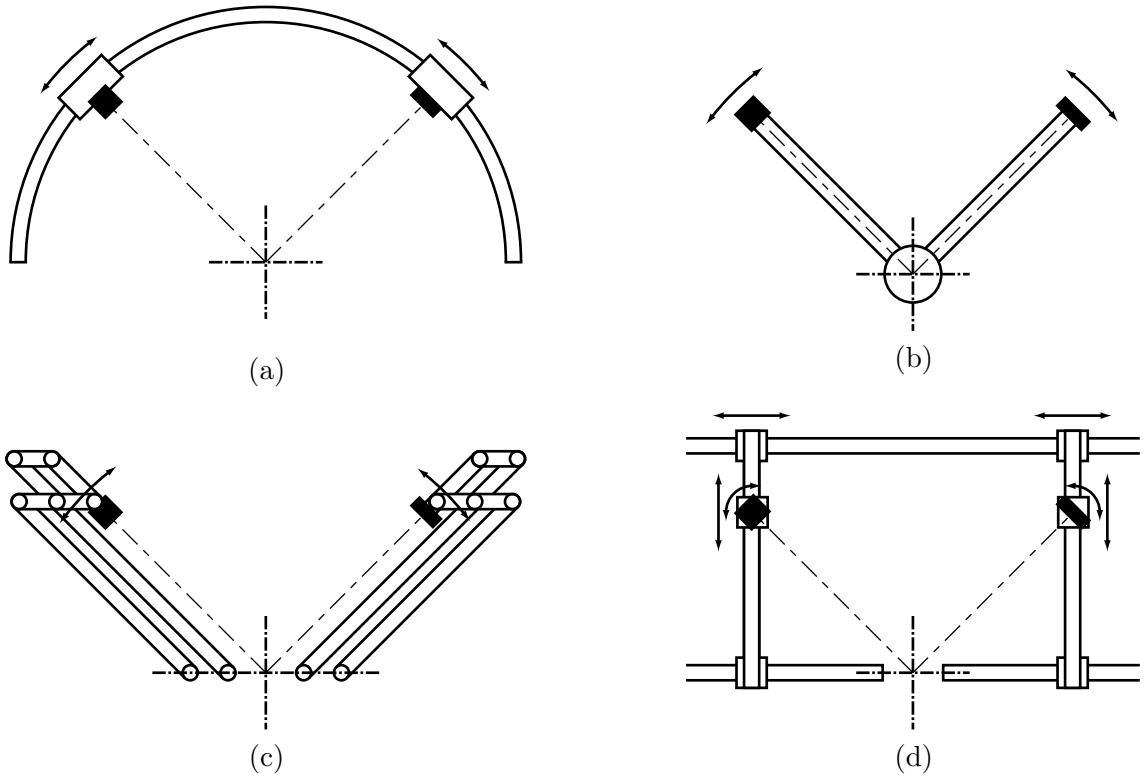

Figure 5.3: motion concepts: (a) guide, (b) rotating levers, (c) rod mechanism, (d) multi-axis mechanism

5.5.1 Guide

In this concept the source and detector are mounted on two carriages which can move along a circular guide. When the carriages move over the guide, the source and detector stay directed at the centre of the circle. When straight linear guides are used (eg. two guides making an angle of 45 ° with the specimen surface) an additional rotation of the source and detector is needed.
The five degrees of freedom are constrained by roller bearings because of their high accuracy and low friction, especially in vacuum conditions. The bearing arrangement is shown in figure 5.4a. Five bearings each constrain one degree of freedom whereas three bearings are used for preloading. Figure 5.4b shows two possible configurations.
Apart from the guide arrangements the concept leaves much space for specimen handling and can provide a robust construction.
The (running) accuracy of the carriage depends on the tolerances of the bearings and the guide and on the 'wheel base' of the bearings. The angle deviation (r_z) is calculated in Appendix

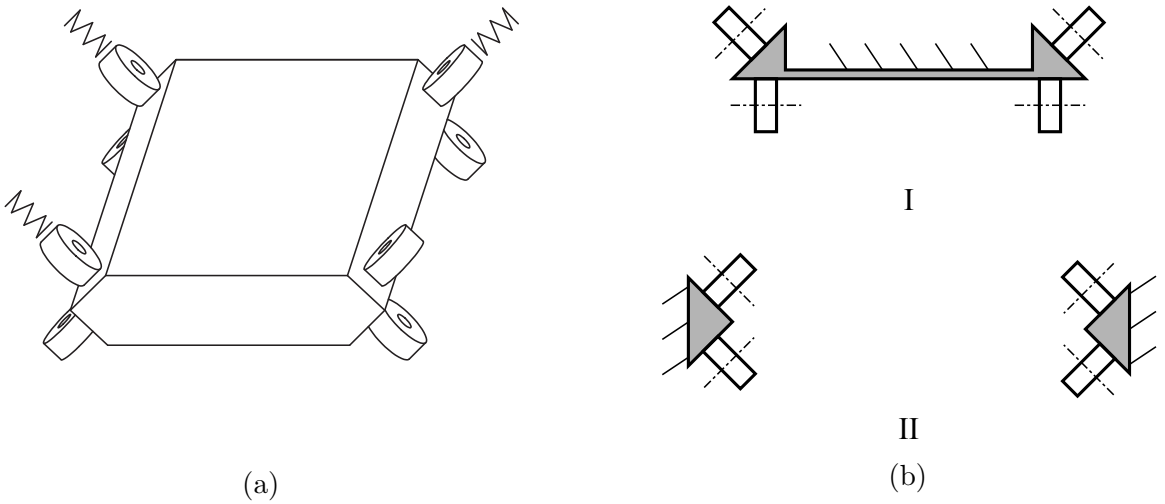

Figure 5.4: guide: (a)bearing arrangement, (b)section views

C.
With a typical radial runout of 1.5 μm for small high precision bearings ([36], [38], [37]), a tolerance of 5μm on the guide [14] and a 'wheel base' of 20mm this means a maximal angle deviation r_z of 140μrad and a radial deviation of 6,5 μm. Increasing the 'wheel base' provides a better angle accuracy but at the expense of mass and, depending on geometry, maximal obtainable angle.

5.5.2 Rotating levers

In this concept the source and detector are mounted on two levers. The mutual axis of rotation of the levers is located on the specimen surface. Physically this means a translation of the rotation axis to the side of the specimen. No additional movement is necessary to keep the source and detector directed at the axis.

The angle and radial (running) accuracy of this concept depends on the radial run-out of the central bearing. With a stacked bearing setup the radial run-out of the inner bearing set will be double the run-out of the outer set. With a radial run-out of 1.5μm the maximum angle- and radial deviation will be respectively:
- 15 μrad and 1.5 μm for the outer shaft,
- 30 μrad and 3 μm for the inner shaft.

5.5.3 Rod mechanism

This concept is based on the previous concept with the difference that the physical rotating axes are moved to the side of the specimen. This leaves more space for specimen handling but adds complexity through the multiple moving parts and pivots. All pivots contribute to friction losses and are a source of deviations. The alignment of the several components gives reason for concern.

5.5.4 Multi-axis mechanism

In this concept the source and detector are positioned by two linear guides and an axis of rotation. The concept gives much freedom of movement (3 degrees for source and detector) and space for specimen handling. However only one degree of freedom is needed and the added functionality is counterbalanced by added complexity and mass. An advantage of this concept is the possibility of correcting misalignment of the specimen.

5.5.5 Concept choice

Criterium	Guide	Rotating levers	Rod mechanism	Multi-axis mechanism
Mass	+	+	+	-
Occupied volume	+	+	+/-	-
Pivots/guides (2D)	2	2	14	8
Accuracy	+/-	+	-	-
Specimen approach (no. of sides)	3	2	3	3

Table 5.1: Estimated characteristics of positioning concepts

Table E.1 gives an overview of the characteristics of the presented positioning concepts. From the presented concepts only the guide and lever concept are seriously viable for the diffractometer. The rod mechanism only has advantage over the lever concept in space for specimen handling. This does not offset the added complexity. The multi-axis mechanism provides lots of freedom in source and detector placement but this does not add functionality. It only adds extra guides, more drives, more motion control and probably more mass.

The guide and lever concept are both good concepts for the diffractometer. In both concepts the source and detector have only one degree of freedom which keeps the number of moving parts, drives and position measurements low. A first mass estimation has given no major difference between both concepts since a substantial part of the mass is enclosed by the supporting structure and parts such as drives and angle measurement. Also the occupied volume will not give large differences.

The distinction will be in running accuracy and complexity. The lever concept has a higher running accuracy. Deviations arise only due to the central bearing unit whereas in the guide concept both guide and carriage contribute to deviations. The values calculated in paragraph 5.5.1 and 5.5.2 show a nine times better angle accuracy and five times better radial accuracy for the lever concept.

Apart from the drive and angle measurement the lever concept will be least complex. Only a central bearing unit is needed to constrain the levers whereas each carriage needs at least five bearings to constrain its degrees of freedom. Additional bearings are needed for preloading. Each bearing contains a risk for possible break-down and subsequent malfunction of the diffractometer.

The main advantage of the guide concept is the freedom in specimen handling since there does not have to be any 'material' near the specimen. The lever concept has the advantage of more freedom in the placement of drives and angle measurement.

Concluding, the guide concept has the advantage of leaving much space for specimen placement. The lever concept, on the other hand, has a better running accuracy, less moving parts (bearings) and more freedom in placement of drives and angle measurement. This leads to the choice for the lever concept.

5.6 Lever layout

The levers can have a symmetrical or asymmetrical layout, see figure 5.5.

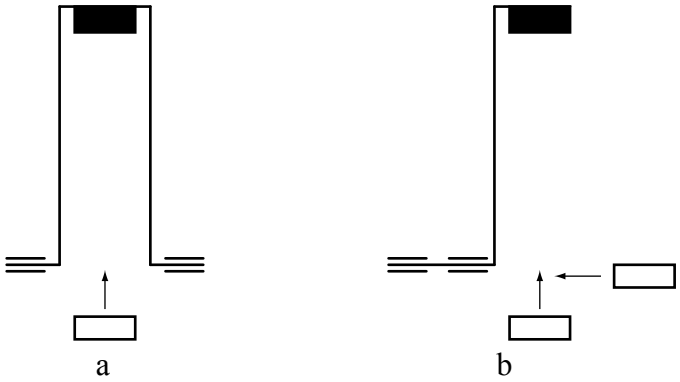

Figure 5.5: lever layout: a) symmetrical, b) asymmetrical

When supported rigidly the symmetrical variant has a higher stiffness to mass ratio than the asymmetric variant. Good bearing alignment is necessary in both concepts but may be easier attained in the asymmetric variant. The mayor drawback of the symmetrical variant is the accessibility of the specimen. The specimen can only be approached from 'below'. This is the main reason for choosing the asymmetric layout.

5.7 Motion

Coupling of movements

It is possible to mechanically couple the movements of the source and the detector. When both levers would only make a synchronous motion towards the normal of the specimen surface, only one drive would be needed. However additional specimen information can be obtained by alternative source and detector positions. Therefore the levers will move independently.

Drive

The levers will be driven on the circumference of the diffractometer circle or on its axes. Alternatively a rod mechanism can be applied to convert a linear movement into a rotational

movement, see figure 5.6.

(a) (b)

Figure 5.6: linear-rotational transmission: (a)vertical drive, (b)horizontal drive

The advantage of this alternative could be a simpler (but indirect) angle measurement and more drive options. However at the cost of an increased number of (moving) parts, added mass, a long force path (with loss of stiffness) and an increased number of friction and play elements.

5.8 Vacuum

On the Mars surface the diffractometer components have to be shielded for contamination due to microdust and hazardous elements in the Mars atmosphere. The radioactive source is of low intensity and intensity is lost due to interaction of the beam with atmospheric elements (scattering). Therefore the diffractometer will be placed in a vacuum box.

5.9 The diffractometer basis

In the preceding sections the choices concerning the system layout are made. This leads to a diffractometer which:

- makes use of the Bragg-Brentano geometry with a radius of 100mm,
- consists of two levers for moving the source and detector,
- is contained in a vacuum box.

The levers will have an asymmetric layout and will be independently driven directly on the circumference of the diffractometer circle or on its axes. The axes of the levers will coincide and be on the specimen surface.

Chapter 6

Design

In chapter 5 the basic system layout is discussed. This chapter presents the final design and the separate components of the diffractometer.

6.1 System design

The diffractometer's final design is depicted in figure 6.1. A baseplate will act as the interface between the Mars-rover and the diffractometer. Mounted on the baseplate, a bearing unit guides the levers of the source and detector. A holder carries the detector/source and a piezo-stepper. This piezo-stepper 'walks' along a guide (=baseplate) thus providing the motion for both levers. The angle position of the levers will be measured by two optical angle encoders. Two shells are welded to the baseplate to provide stiffness and to protect the diffractometer instrumentation from the Mars environment. A beryllium window provides passage for the X-rays.

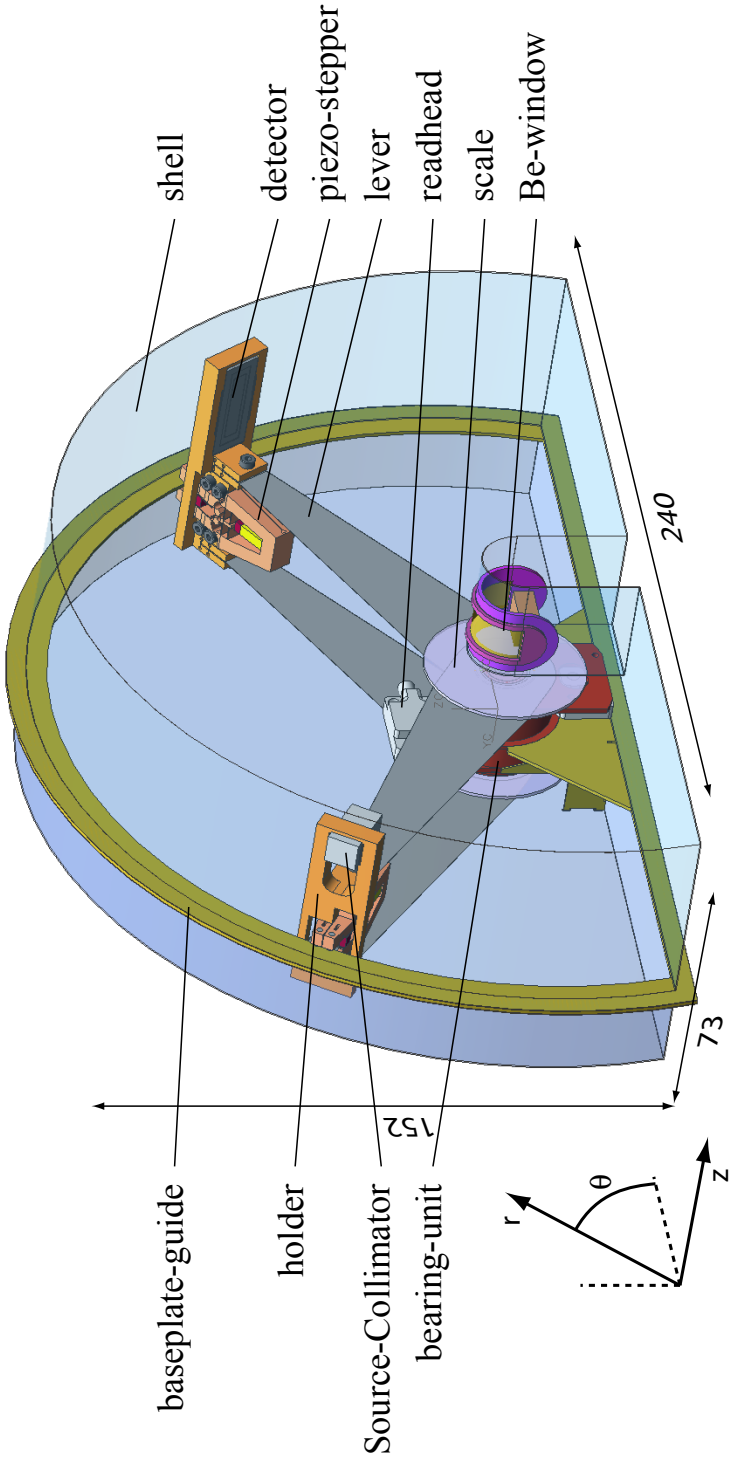

Figure 6.1: Final diffractometer design

6.2 Source and collimator

The x-ray source will be a radioactive Fe55 line source. The main advantages of a radioactive source are the production of monochromatic radiation, the lack of input power and its minimal size in comparison to an x-ray tube. Due to the lack of input power no significant heating of the source occurs. The disadvantages of a radio-active source are the low intensity and its decrease in time and the relative large thickness of the line source. Also the handling of radioactive sources needs extra precautions. Because the radioactive source emits monochromatic radiation no filter is needed. To direct the beam a collimator will be used. Probably this collimator will make use of pore optics or capillary tubes.

6.3 Detector

The diffractometer is expected to make use of a high purity Ge-strip detector. This solid state detector does not need the cooling a Charged Coupled Device (CCD) needs to minimise the 'dark current'. It is a lightweight, small detector which can withstand the required temperature range [16]. The detector is directly mounted on a multichannel ASIC (Application Specific Integrated Circuit) in order to minimise noise. Because of its small pitch the detector itself functions as a slit. Therefore the receiving slit can be omitted. For the design the dimensions of the detector are based on the Atmel TH7814A CCD.

6.4 Actuation

The lever can be actuated at its axis or on the circumference of the traced circle. When actuating on their shafts, the levers (initially) only carry the detector and the source. This means a low moving mass and no additional heat sources on the lever. However when actuating on the circumference of the traced circle, the actuation stiffness, accuracy and resolution will be higher. Therefore the lever will be actuated on circumference of the traced circle.

6.4.1 Actuators

This paragraph presents potential actuators for the diffractometer and the choice for one of them.

Electronically commutated/stepper motors

Electronically commutated (EC) and stepper motors are already applied in space. By the use of a gear and a rack or a friction wheel the motor motion can be transferred into motion of the lever. The stepper and EC motors need a considerable reduction to provide sufficient torque. This introduces play, loss of output power and generation of heat. EC motors have no detent torque whereas stepper motors have only a minimal detent torque.

Linear motor

Linear motors show high accuracy and avoid motion disturbances due to nonlinearities, such as friction, backlash or pitch errors, which occur with conventional mechanical gears and rotating servomotors [27]. However a linear motor shows a considerable heat development

due to copper losses and magnetic forces perpendicular to the feed direction. The linear motor presents no holding force when switched off.

Ultrasonic motors

Ultrasonic motor is a general term for a variety of actuators. A classification can be found in [28]. Ultrasonic motors use mechanical vibration and frictional force between solid materials. The mechanical vibration is excited by piezoelectric material in a transducer. Usually, ultrasonic motors are operated at a resonance frequency of tens of kilohertz. Ultrasonic motors feature high output force and are suitable for high-speed and high-resolution positioning systems. No lubrication is needed. However, for precise positioning the stator of an ultrasonic motor must be rigidly held. As the stator itself vibrates, the holding mechanism of the stator is frequently a problem [25]. Frictional losses are large owing to the complex nature of the vibrations. Besides motor performance is dependent on many factors such as material combinations, temperature, preload and frequencies. The holding force of ultrasonic motors will be dependent on the type of motor.

Surface Acoustic wave

A surface acoustic wave (SAW) motor can be seen as an ultrasonic motor but it uses nanometer order vibration instead of micrometer order for friction drive [26]. The advantages are its high resolution and the absence of lubrication. The latter makes it suitable for vacuum operation and the blocking of motion in absence of waves. However not all observed phenomena are fully understood yet [24]. The principle is promising but yet not completely 'mature'.

Stepper

A stepper displays a discrete motion. The actuated body is clamped, set up and then overtaken by another clamp. When piezo's are used for motion, sub-micrometer steps are possible. The principle of a piezo stepper is not new. Burleigh has a commercially available linear stepper, the Inch-worm [17]. D.M.H. Philips for his master thesis [41] and engineers at AMOLF [18] both have developed a rotary piezo stepper, the latter for ultrahigh vacuum. A piezo stepper features a potential high actuation stiffness and high holding force. Due to the intermittent motion power-consumption can be low.

Actuator choice

The stepper-, EC- and linear motor need continuous power supply to keep the lever in position. This means continuous power dissipation and thus heat generation. The performance and functioning of a surface acoustic wave motor is dependent on many factors. This implies possible risks which should be avoided in space operation. For the same reason SAW motors are not a serious candidate for the diffractometer yet. The piezo stepper main disadvantage is the motion discontinuity at clamp change (due to over-constrained positioning).
When comparing the actuators the drawbacks of the piezo stepper are the least troubling. At the same time it potentially has high holding force,high actuation stiffness, sufficient resolution and low power consumption. None of the other actuators have the same benefits. Therefore a piezo stepper will take care of the actuation of the levers.

6.4.2 Stepper design

As mentioned in paragraph 6.4.1, D.M.H. Philips and AMOLF already developed a rotary piezo stepper. Both designs actuate a disk over 360 degrees.
The levers of the diffractometer only have to be actuated over 180 degrees. A full 360 degree disk would take too much space. Therefore the stepper will, in contrast to the mentioned designs, be mounted on the lever and will step along a guide. The levers will be fixed when no power is supplied. This avoids damage due to electric disturbances, saves power and makes locking during idle time superfluous.

The stepper consists of two clamps with an actuator between them.

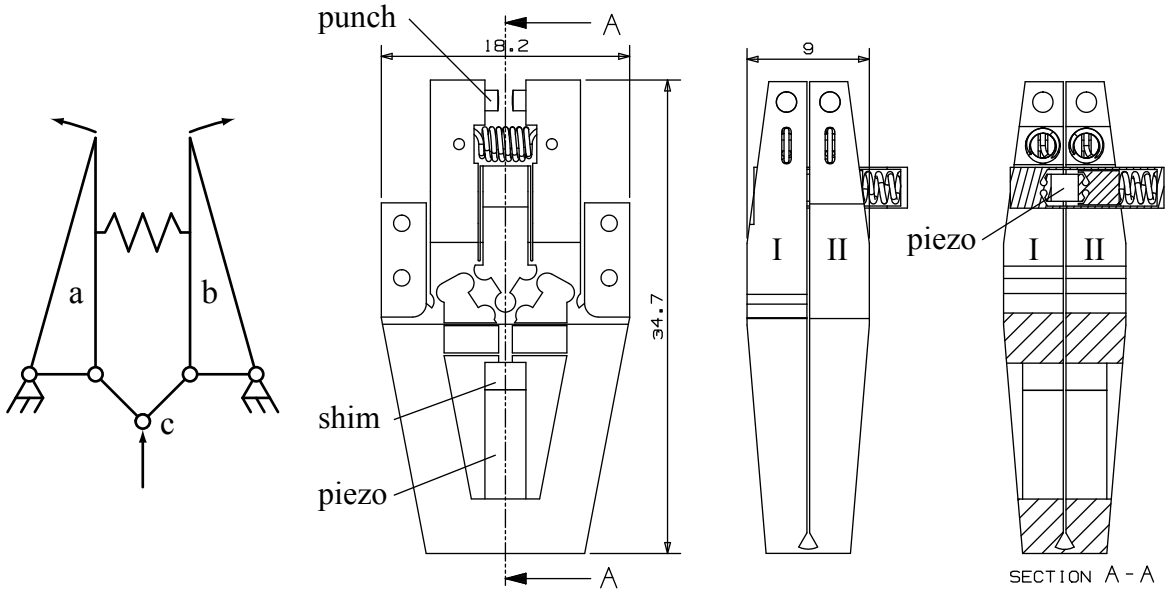

(a) (b) (c)

Figure 6.2: Piezo stepper

The basis of the clamp is a synchronised motion of two levers (a and b in figure 6.2a) due to a linear input (at c in figure 6.2a). This mechanism can be discerned in figure 6.2b, the front view of the actual clamp. Pivots are realised by elastic hinges. Elastic hinges do not display play, hysteresis, friction and wear. Two parallel plates make up a linear guide. A piezo takes care of the motion.
The advantage of piezo's over other actuators are its high compactness, large force generation, the absence of friction and Ultra High Vacuum (UHV) compatibility. The used piezo's feature a low operating voltage and a high Curie Temperature (320°, required for baking out). The specifications are listed in appendix E.6. For more information on piezo principals the reader is referred to [6].
A synchronised motion of the two levers avoids friction in the moving clamp since both punches are released and total clamp stroke is doubled because one actuator actuates two levers. In this way a 1:6 transmission ratio can be obtained. The calculated transmission ratio is 7.4 but some stroke is lost in the structure due to elastic deformation. Appendix E

shows the stepper calculations and appendix G the Finite Element Analyses. When the piezo is idle, a spring closes the clamp. Actual clamping is realised by two punches with rounded tips. Possible materials for this contact are given in appendix E. The calculations are based on Silver/MoS_2 versus silver plated steel contact.

Between the piezo and the linear guide a μm gap facilitates free movement of the clamps. The stepper is machined by wire EDM and milling.

For step motion two clamps (I and II in figure 6.2c) are combined and moved by another piezo. The step motion consists of six steps:

- clamp I is closed and clamp II is released,
- the piezo expands and moves clamp II,
- clamp II closes,
- clamp I is released,
- the piezo retracts,
- clamp I closes and clamp II can be released again.

The motion does not fully comply the preferred motion (along the guide) but due to its small stroke, deviations are assumed to be corrected by the radial stiffness of the construction.

Piezo's are very sensitive to tensile forces and bending forces. To avoid bending forces the piezo and the clamp are connected by an elastic hinge. The maximal tensile load of the motion piezo is 5N. During stepping operation this value will not be exceeded but under 40g acceleration the inertial force can be 10N. Therefore a preload is applied by means of a compression spring.

6.5 Lever design

The levers have to rotate around a mutual axis. This axis is defined by a bearing set. One set of bearings for each lever constrains five degrees of freedom (DOF). Only one degree of freedom, θ, is left unconstrained.

The levers are actuated by a piezo stepper. This stepper also constrains two DOF (z and θ). To avoid an over-constrained lever, one DOF has to be released. By using two parallel placed leaf springs (each constraining three DOF) for the lever, the DOF in z direction is released again. However within the lever the rotation around z, r_z, is constrained twice if the stepper-unit were rigid. However the stepper-unit has low torsional stiffness and an internal DOF is assumed. Figure 6.3 shows two parallel placed leaf springs in side view (parallelogram). A relative large displacement in z only leads to a small displacement in r:

$$\Delta r = \frac{\Delta z^2}{2L} \tag{6.1}$$

The leaf springs are mounted on both ends of the shaft in order to create distance between the leaf springs, thus creating higher rotational stiffness in the r-z-plane.

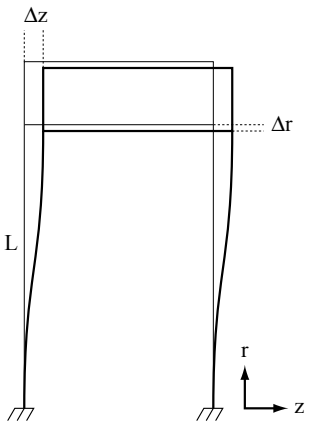

Figure 6.3: Parallelogram

6.6 Detector/source mounting

The stepper and source/detector are mounted on a holder (figure 6.4). This holder is mounted on the two leaf springs thus providing a stiff interface between the motion element, the motion guide and the detector/source. To avoid high stresses due to differences in the coefficient of thermal expansion between the holder and the source/detector, three slits are introduced at the mounting points of the detector/source.

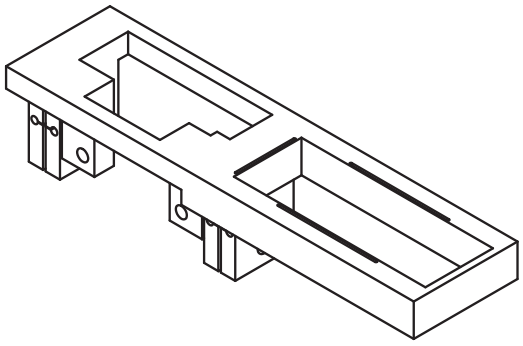

Figure 6.4: Detector holder

6.7 Bearing design

The bearing-set is the interface between the levers and the box. The levers take care of source and detector positioning. Therefore their axis of rotation should be well defined. Both levers rotate around a mutual axis. For the diffractometer this means that the bearings are stacked. A stacked bearing set displays high parallelism and concentricity.

Figure 6.5 gives three configurations for mounting the bearing-set on the box. The levers are mounted on the moving bushes or shafts.

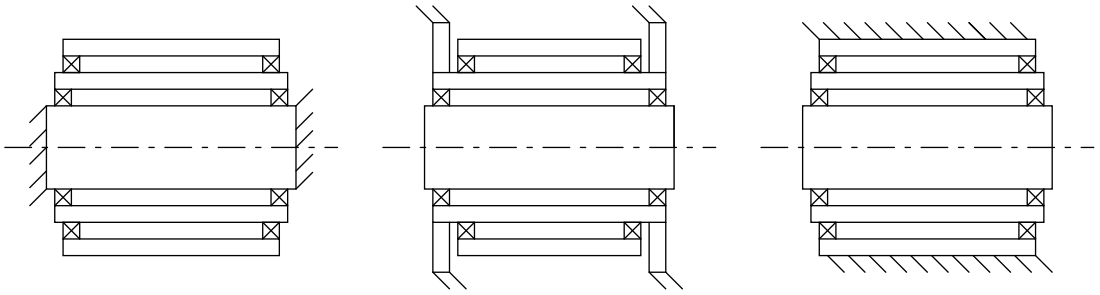

Figure 6.5: Bearing configurations

Configuration (c) is used in the diffractometer. The main advantage of this setup in comparison to the other two configurations is the possibility of mounting auxiliary equipment on the bearing housing. In the diffractometer design this means a more compact design and possibly lower mass. In comparison to configuration (a) the bearing setup will provide higher stiffness since the moving bushes are stacked on its largest bearing pair. Configuration (b) has advantage over (c) in calibration data interpretation because there is no dependency between the two moving bushes.

6.7.1 Bearing type

Angular contact ball bearings are used in the diffractometer. Rolling element bearings feature lower friction and wear relative to sliding element bearings. A set of angular contact ball bearings provides radial stiffness in combination with axial stiffness. When preloaded, high running accuracy can be obtained.
An alternative to ball bearings could be a magnetic bearing. Magnetic bearings provide high accuracy but active control is needed. This would mean a substantial increase in mass and complexity.

6.7.2 Conventional bearing layout/ integrated bearing

The bearing unit can consist of standard bearings but the bearings can also be integrated in the housing and shafts. The bearings in the design are integrated because integrated bearings have several advantages over a conventional design.
Integrated bearing units offer running accuracies according to ABEC7 to ABEC9 (ISO tolerance class 2 to 4) [19]. Because of a lower number of components there are less tolerances and fitting- and centring faces. Misalignment of the inner ring is not possible and the increase of shaft diameter increases stiffness. Integration of the bearings gives freedom in dimensioning and can lead to mass and volume reduction. The disadvantage of integrated bearings are the added engineering effort and costs.

6.7.3 Preload

Preloading makes it possible to increase both bearing stiffness and the arrangement's running accuracy. Single row angular contact bearings are adjusted against each other by axial displacement of the inner or outer rings until a certain preload or clearance is obtained in the bearing arrangement. Preload can be position- or constant pressure preload. Position preload is realised by using spacers or shims to obtain the required spacing and preload. Position preload provides great axial stiffness but has some drawbacks [29]:
- If 'peelable' shims are used for preload setting there is potential for loss of preload over time due to adhesive or material creep.
- There may be high uncertainty over the actual preload set.
- Large variations in preload during thermal vacuum testing due to mismatch of thermal expansion coefficients at soak temperatures and under thermal gradients.

Under constant pressure preload it is possible to minimise any change in preload. Constant pressure preload is realised by the use of a spring, e.g. leaf spring or coil. The variation of spring load with shaft/housing expansion and contraction is negligible. The bearings in the diffractometer will use constant pressure preload.

6.7.4 Bearing materials

Bearings with steel balls and raceways can give problems in vacuum. Under marginal or non-lubricated conditions the asperities or peaks of each surface contact under high localised stress and temperature. During bearing operation asperities weld and break. This causes damage and contamination. The diffractometer will make use of ceramic balls on steel raceways, i.e. hybrid bearings. Ceramics sliding or rolling on steel do not generate high adhesion force or microwelds at the asperity contacts. They show a lower coefficient of friction than steel-steel contact and have relatively low adhesive wear. Other advantages are the low mass of the ceramic balls and the longer fatigue life [30]. A disadvantage is the relative high cost of hybrid bearings. Ceramic bearing balls are typically made of Silicon nitride but ruby (sapphire) is also used. Ruby has a higher modulus of elasticity (higher stiffness) and a coefficient of thermal expansion nearer to steel. Therefore ruby balls are used.

6.7.5 Lubrication

Because of its vacuum operation liquid lubrication is not desirable. Instead of a liquid or grease solid lubrication is used. The best options for solid lubricant films for space applications appear, at present, to be ion-plated lead and ion-sputter deposition of, and/or ion-assisted deposited, MoS_2 [7]. These lamellar films have demonstrated very low friction operation in sliding and/or high low-load rolling bearings and latch and release mechanisms. Sputter-deposited MoS_2 has a lower coefficient of friction than the alternative, ion-plated Pb (0.01 vs 0.1), which means that MoS_2 components should develop less torque. The use of MoS_2 is presumed for the diffractometer bearings. Alternative solid lubricants are shown in appendix D. Because solid lubrication can give irregularities no lubrication can be an option. The ceramic-steel bearing does not tend to microweld and ceramic on steel shows a low coefficient of friction.

6.7.6 Design integrated bearing

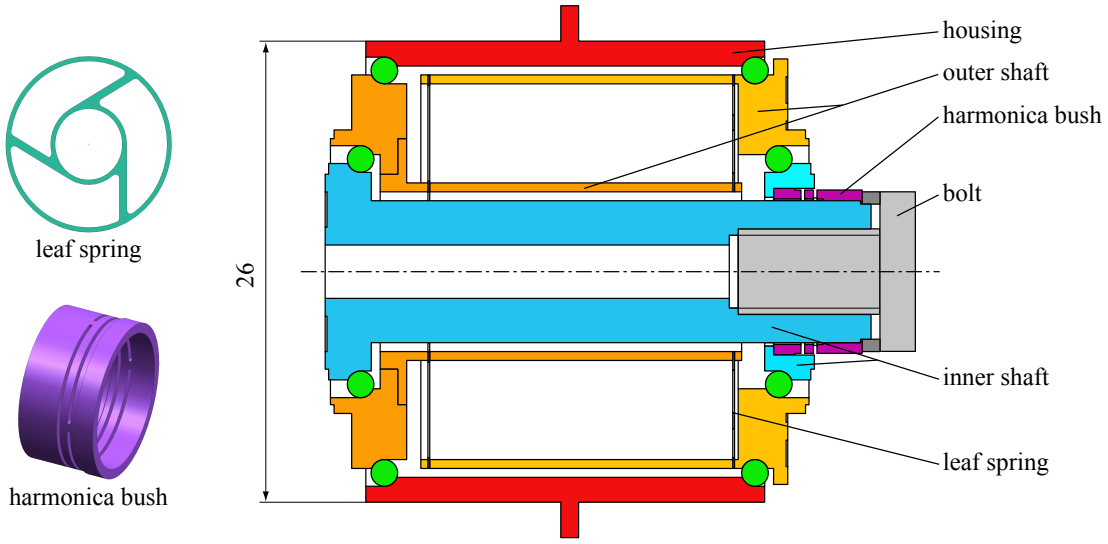

Figure 6.6: Integrated bearing setup

The layout of the bearing is shown in fig 6.6. The outer shaft rotates in the housing. Within this shaft, the inner shaft rotates. Since a deviation in the angle of incidence of the x-rays causes both a diffraction error and read-out error, the lever of the source is mounted on the outer shaft. The bearings of this shaft display higher stiffness and less radial run-out (no stacked run-out).
To avoid mass and volume, and to enable the placement of the levers near the pole of the bearings, the bearing unit will be preloaded by one preloading element. In order to preload the outer bearing set the outer shaft needs an axial degree of freedom. This is realised by dividing the outer shaft in two parts. These parts are connected by two leaf springs which constrain all degrees of freedom except the axial one. Alternatively a sliding bush could be used to release the axial degree of freedom but a sliding bush would need an additional coating to avoid cold-welding and would introduce play.
The inner bearing set will be preloaded with the use of a spring bush, also called harmonica bush. This bush can be seen as a cardanic joint with low axial stiffness. When the pole of the mounted harmonica bush coincides with the pole of the angular contact bearings, no moments will be transferred and the five degrees of freedom of the shafts are constrained. With the use of a harmonica bush no sliding fits are needed thus increasing accuracy and decreasing the possibility of cold weld between the sliding parts.
Preload increases bearing stiffness and accuracy but also increases the friction torque and contact stresses. Therefore the preload should not be to large. The minimal preload is defined by the launch forces. The mass of the shafts and the levers experience a acceleration of 40g. To avoid movement of the shafts the bearing preload should at least equal the experienced axial load.
The mass of the levers and the shafts is about 40g. This creates an axial force of 16 N. In accordance with ECSS-E-30-3 the safety factor for inertia, 1.1 and spring, 1.3 have to be

applied. This results in a minimal preload force of 21N. This is the minimal preload force. The applied preload force is chosen to be 25N.
The axial stiffness of the leaf springs is $2.5 \cdot 10^3$ N/m. With an assumed maximal displacement of 0.1 mm this leads to a maximum reaction force of the two leaf springs of 0.5 N (Appendix G).
Bearing races are manufactured with a race conformity $R_r = \frac{r}{d}$ in the range $0.51 \leq R_r \leq 0.54$ [30]. A higher race conformity reduces friction but on the other hand results in higher contact stresses. For the bearing calculations (appendix D) a conformity of 0.53 is used. With the current full race setup no ball-cage is needed.
The static load rating of the inner and outer bearing is 243N and 514N. When all the inertial forces of the levers including clamp and detectors would be applied on one bearing, a static load rate of about 70 N would be needed.

6.8 Angle encoder

For measuring the angular position of the source and detector the diffractometer needs angle encoders. Two types of angular encoders are suitable for long stroke and high resolution and accuracy and are accepted in space applications.
The first option is the Inductosyn^{TM} [9], a multipole resolver. The Inductosyn is already used in space applications. Its measuring principle is based on inductive coupling between windings on a rotary or linear pair of elements. Appendix H describes the operating principles in further detail. Advantages are a rugged design, high accuracy and resolution. A possible advantage is the integration the Inductosyn in the design. The windings of the stator can be etched on the guide of the stepper thus saving mass.
The Inductosyn is promising but no support could be found from the supplier. At the moment not enough information is available to use or integrate the Inductosyn in the design.

The second option is an optical encoder. The encoder consists of a readhead and a scale. Lightweight scales include a disk scale or a tape scale. For accurate angle measurement the angle of the detector and source is preferably measured as near as possible to their position, on the diffractometer circle. Measuring at a large radius has the additional advantage of higher resolution for the same grating period. However for the diffractometer it has considerable disadvantages. A tape scale is a very lightweight and easy to integrate scale option but no small readheads are available. This would imply increased lever dimensions, mass (inertial forces) and possibly a smaller maximum diffraction angle. Moreover the cable of the readhead disturbs the lever motion because of its relative stiff mounting to non-moving parts. Solutions to this problem will increase complexity. Using a disk scale, the same problems arise and extra mass is added due to the large radius of the scale and its mounting on the side of the box.

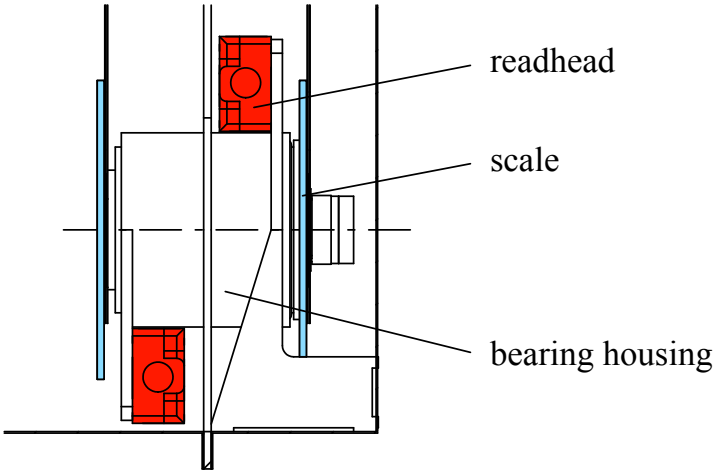

Figure 6.7: Position of scales and readheads

To avoid the preceding problems the readheads are mounted on the non moving parts. A scale is mounted on the shafts of both the levers, see figure 6.7. The readheads can be mounted on the shell or on the bearing housing. Mounting on the bearing unit provides a stiffer mount in axial direction. The mounting face of the readhead also makes mounting on the bearing housing an obvious choice. This leaves the shell to be only a structural element without the need of high tolerances.
Appendix H gives the specifications of the used encoder and scale.

Redundancy

The angle-encoders measure the angle of incidence and the angle of diffraction. Since the stepper makes a constant step, as does a stepper motor, counting the steps from a reference point will also give the angle information. Tests should give information on the reliability of this method. The angle encoder will be calibrated (on site) by a specimen of known compound. This in itself also gives the necessary angle information (interpolation between known diffraction peaks) but some kind of redundancy is not superfluous and will give back-up data.

6.9 X-ray window

The specimen is located outside the box. To be able to radiate the specimen the box needs an X-ray window. An X-ray window is made of beryllium foil with thicknesses in the range of 10 μm. The diffractometer window will cover 180° with a width of 10 mm. Transmission of X-rays through a 10μm foil is about 90 % [3].
The beryllium foil has to be bonded to the box. Figure 6.8 gives suggestions for a welded interface. No appropriate information could be found on welding beryllium to steel. Therefore test should be conducted to investigate the possibilities. Option I supposes the welding of the foil directly on parts of the box. Optionally the foil first can be welded between two relatively

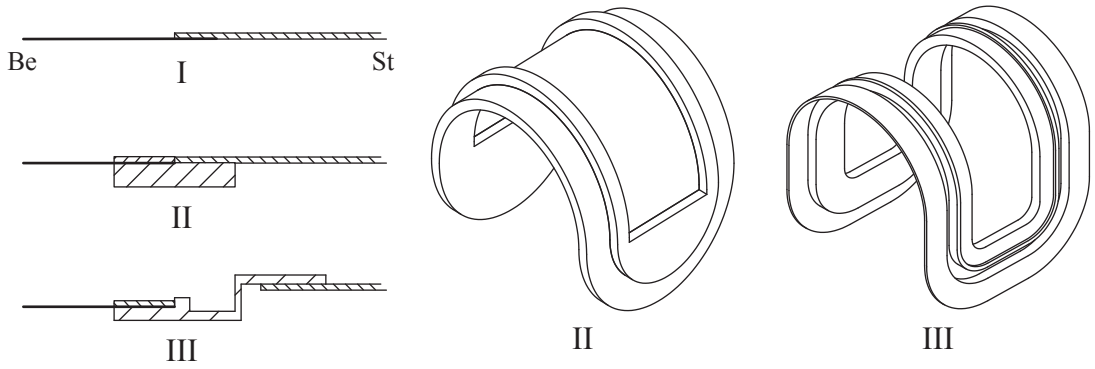

Figure 6.8: X-ray window

thick brackets which subsequently can be welded on the box (option II). Maximal material stresses due to differences in thermal expansion during space flight will not be exceeded (see Appendix F).

Alternatives to welding can be vacuum furnace brazing or diffusion bonding. Diffusion however needs precisely mating surfaces and may give problems with curved surfaces. Vacuum furnace brazing takes place at high temperatures. Option III features a groove in order to minimise the increased (in comparison to welding) thermal stresses. The raised edge works like a spring on the beryllium foil.

6.10 Box

The box consists of two shells welded to the baseplate. A welded joint, in comparison to a bolted joint, does not add additional parts and mass. A disadvantage is that a welded box can not be disassembled without damaging the box.

The shells are made up of welded steel sheet parts. Alternatively, the shells can be weldless by deep drawing the shells.

The box is not designed for vacuum conditions on earth. The pressure on the flat sides asks for severe structural reinforcements which will increase the diffractometer mass and which will be redundant in space or on Mars. The use of a valve is supposed. In this way space itself will act as a vacuum pump. The valve will close before entering the Mars atmosphere. The box can be filled with helium on earth to avoid any contamination due to elements in the earth atmosphere. Remaining Helium has little influence on the beam of X-rays.

The box as depicted in figure 6.1 has too low an eigenfrequency. For the spaceflight model the flat sides of the box need reinforcement to avoid permanent damage during launch. Reinforcements can be made up of ribs or of sandwich constructions. Appendix G shows how the eigenfrequency of the box is increased from 68 to 321 Hz by adding stiffeners. The increase in mass is about 15g.

6.11 Diffractometer - rover interface

The orientation and mounting options in the rover are not known yet. To constrain 6 DOF with a thermal centre on the diffractometer axis three hinged leaf springs are suggested. Figure 6.9 shows two options for leaf spring positions.

The left option provides a stiffer support for the bearing unit and a more uniform stiffness in the $\theta - r$ plane but the rover interface will define the possibilities.

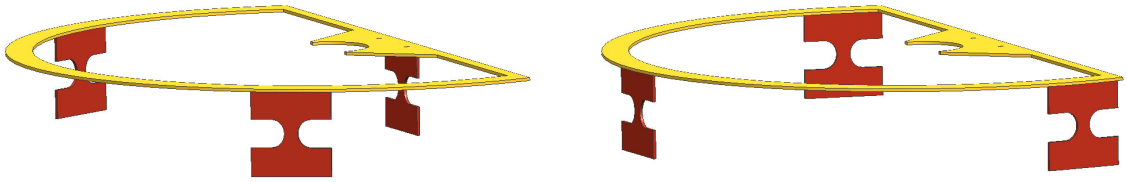

Figure 6.9: Diffractometer-rover interface

6.12 Launch-lock

The clamps fix the position of the levers during operation. The experienced accelerations are relatively low ($5 m/s^2$) and only a small clamping force is needed. During launch however the experienced accelerations are high and the inertial forces exceed the holding force of the clamp. To fix the levers during launch a launch-lock is required. The eigenfrequency of the 0.15mm thick leaf springs is 100 Hz (see Appendix G), which is too low for launch. To withstand launch the levers can be reinforced as shown in Appendix G or again, a launch-lock could constrain the leaf spring motion.

A launch-lock is not provided yet. R.A. Veugen in his thesis report [40] discusses some commercially available mechanisms which are applicable to the diffractometer. The holders of the source and clamp can be fixed by inserting a pin in the holder. This pin fixes the θ direction. The r and z direction are already fixed by the levers and the guide. When descended on Mars a release mechanism retracts the pin and sets the levers free.

The leaf springs can be supported by a polymer wire (e.g. kevlar) which supports the leaf springs normal to its face. When descended on Mars a thermal knife melts the wire and sets the leaf springs free. A spring at the end of the wire retracts the wire. Alternatively a spring loaded 'Guillotine' can be used in combination with a steel wire. The wire curls up when cut.

The polymer wire can give problems with the planetary protection policy. The 'Guillotine' adds complexity and moving parts.

An alternative without moving parts can be a docking station. When launched the levers are placed in an end position. In this position the leaf springs are supported in z direction by small plain bearings.

6.13 Materials

To avoid stresses and deformation due to differences in the coefficient of thermal expansion the diffractometer is as much as possible made of one material. TiAlV and steel are suitable and widely used materials for space applications because of their high strength and stability. TiAlV has the advantage over standard steel in having a higher yield stress and lower density. However its machinability and weldability is poor in comparison to steel [15] and the yield strength of various steels equals or exceeds the yield strength of TiAlV. Therefore steel is chosen to be the base material. Aluminium is not considered because of its low yield strength and low hardness, which makes it unsuitable for bearing raceways.
Suitable steels ([33],[1]) are the low carbon stainless steels in the AISI 400 series (e.g. 431), maraging steels and some precipitation hardened steels (e.g. 17/7PH). These steels have thermal expansion coefficients from 10 to 11 μm/m°C. Exact material specifications have to be defined, based on their properties and availability. Calculations are based on maraging steel 18Ni1700.
To avoid cold-welding, mating surfaces of motion elements are made of dissimilar materials. As mentioned in paragraph 6.7.4 the bearing balls are ceramic. For the punch-guide contact Silver/MoS_2 versus silver plated steel is assumed.

6.14 Assembly

6.14.1 Bonding

Welding

All steel subassemblies will be welded. Welding provides a strong bond without adding mass and parts. For the the vacuum tight parts micro plasma arc welding is suggested. Other parts can be welded with laser welding. The possibilities of welding the beryllium window have to be investigated but electron beam welding can be an option.

Glue-ing

The piezo's, scales, detector and source are intended to be glued. Special glues have been developed for use in space. Care have to be taken with the presence of X-radiation. The influence of the X-radiation has to be investigated since most glues are not X-radiation resistant. Shielding of the glue may solve the problem. Otherwise soldering or (vacuum) brazing can be taken into consideration

Fits

The shaft components of the bearing and the harmonica bush will have a tight fit.

6.14.2 Alignment

The elements in the diffractometer are not adjustable. Introducing adjustment elements would mean an increase in complexity and mass. For alignment of the various components an external alignment tool has to be designed. The detector and source have to be aligned according to table B.1.

The piezo clamp is designed with high tolerances. Especially the gap between the piezo actuator and the linear guide is critical. By using a dummy guide the distance between the piezo and linear guide can be measured and a fitting shim can be machined.
The alignment of the source and detector needs attention when more is known of the actual dimensions, shape and reference possibilities.

Chapter 7

Evaluation

This chapter reviews the characteristics of the diffractometer.

7.1 Performance

7.1.1 Dynamic operation

Due to accelerations and corresponding inertial forces the stiffness of the actuator components is of major importance. When all stroke is lost in deflection of the components, no movement will take place. To avoid loss of stroke the components are assumed to need about ten times the stiffness which would give a zero stroke at maximal acceleration.

During step motion the movement of the clamps relative to each other and the movements of the clamp levers are of importance. The required stiffness is estimated by:

$c = 10 \cdot \frac{F_{max}}{u} = \frac{10 \cdot m \cdot a_{max}}{u}$.

The mass to be moved is 50g, the maximum acceleration is assumed to be $5 m/s^2$ and the stroke $1.5 \mu m$. This results in a required stiffness of $1.6 \cdot 10^6 N/m$ in motion direction.
Figure 7.1a shows the results of the FEM analysis on the stepper clamp. The stiffness of the clamp is calculated: $4 \cdot 10^6 N/m$. The two clamps have a serial stiffness of $2 \cdot 10^6 N/m$.

The movement of the levers of the clamp are important for releasing the clamp off the guide. When considering one side of the clamp, the moving mass is the mass of the lever, 5g. When the mass will be considered a point mass on the punch, the reduced mass of the lever will be $\frac{1}{3}$ the mass of the lever. Because of a 3:1 reduction of the stroke the mass 'seen' by the piezo will be 9 times the reduced mass: m'$= 5g \cdot \frac{1}{3} \cdot 9 = 15g$. With a stroke of $3 \mu m$ this results in a required stiffness of $1.2 \cdot 10^5 N/m$.
Figure 7.1b shows the FEM analysis on the clamp levers. The calculated stiffness is $1.1 \cdot 10^6 N/m$.

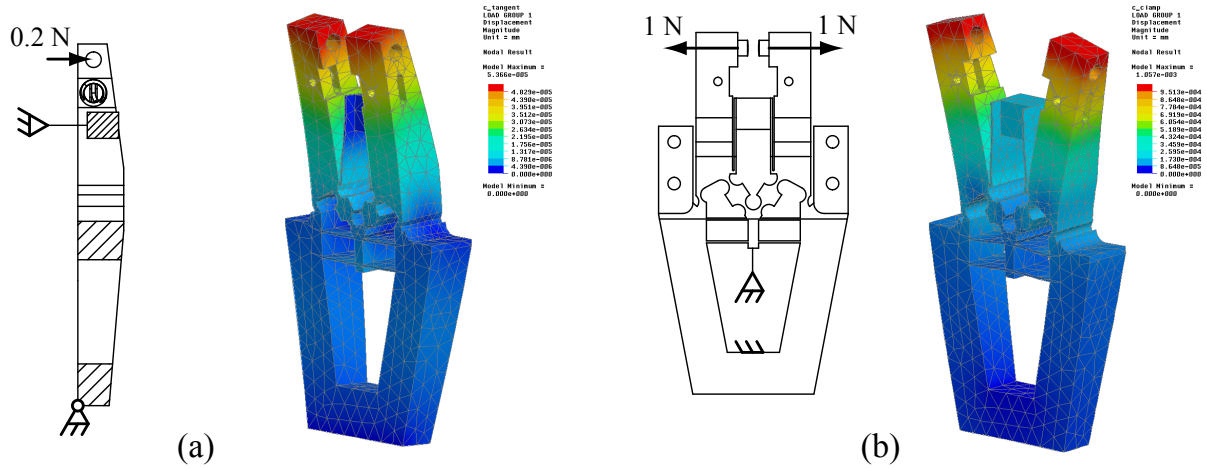

Figure 7.1: (a) Stiffness in motion direction, (b) Stiffness in the clamping mechanism

7.1.2 Actuating stiffness

For high accuracy the actuating stiffness should be high. Because the stepper has a closed force loop, the stepper is considered to be independent of the levers. Because the stiffness of the elastic hinge ($c_x = 2.8 \cdot 10^8 N/m$) is about 10 times the stiffness of the piezo ($c = 3.62 \cdot 10^7 N/m$) the hinge is considered to be a fixed joint.
A simple model for calculating the actuator stiffness is shown in figure 7.2. The motion and stiffnesses in the model are linear.

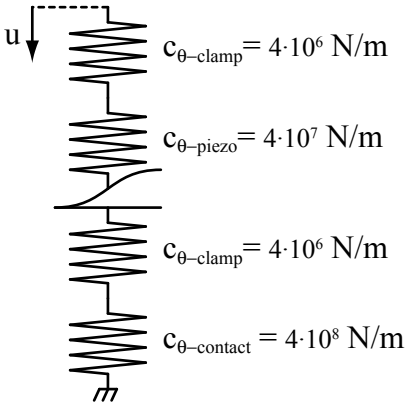

Figure 7.2: Actuating stiffness

$c_{\theta-clamp}$ is the stiffness of the stepper levers, determined with the help of a FEM tool (figure 7.1a).
$c_{\theta-contact}$ is the contact stiffness in the punch-guide contact, calculated in Appendix E.
$c_{\theta-piezo}$ is the piezo stiffness.

It can be seen that the contact stiffness and the stiffness of the piezo are at least ten times the stiffness of the clamp lever. Therefore the model can be reduced to the serial stiffness of the clamp levers:

$$c_{out} = \frac{1}{\frac{1}{c_{clamp}} + \frac{1}{c_{clamp}}} \tag{7.1}$$

which results in an output stiffness of $2 \cdot 10^6 \mathrm{N/m}$.

Virtual play can have a negative influence on the accuracy of the stepper. With the calculated output stiffness and a negligible friction moment in the bearings (GRW [36] and Myonic [37] estimate a friction moment in the order of magnitude of a few tens of $\mu \mathrm{N} \cdot \mathrm{m}$) this will be negligible for the diffractometer.

7.1.3 Running accuracy

The position of the source and detector is defined by the bearing set. The radial and axial run-out have to be measured. A similar bearing setup for one shaft with commercially available high precision bearings and a spring bush for preloading, showed a radial run-out of 0.5 μm [22]. The axial run-out for high precision bearings is typically 1.5 μm. The radial run-out determines the angular deviations $\mathrm{r_r}$, r_θ, $\mathrm{r_z}$ and the displacement Δr. The axial run-out determines the displacement Δz.

When assuming a radial run-out of 0.5 μm for a single bearing set, the maximal radial displacement Δr of the source and detector will be 0.5 and 1 μm.

The maximal angular deviations $\mathrm{r_r}$ and r_θ are found by dividing two times the radial run-out by the bearing distance (22mm) and will be 45 μrad for the source and 90 μrad for the detector.

The maximal angular deviation $\mathrm{r_z}$ is found by dividing the radial run-out by the distance between the source/detector and the axis of rotation (100 mm) and will be 5 μrad for the source 10 μrad for the detector.

The maximal displacement Δz due to axial run-out will be 1.5 μm.

The angle resolution of the source and detector is 15μrad when the stepper makes steps of 15μm. The resolving power of a diffractometer $\frac{d}{\Delta d}$ depends on the angle θ and the angle resolution $\Delta\theta$:

$$\frac{d}{\mathrm{d}d} = \frac{-1}{\mathrm{d}\theta} \tan\theta$$

To compensate for loss in resolving power at low angles, the resolution can be increased by making smaller steps.

The stability of the source and detection position is mainly determined by temperature influences. Because of the symmetrical setup of the lever, clamp and holder, position deviations in motion direction due to thermal expansion are negligible. In radial direction the detector will move maximally 0.7 μm during one run.

7.2 Thermal considerations

During space flight the diffractometer experiences temperature changes up to 200° Celsius. To avoid stresses and hysteresis due to differences in the coefficient of thermal expansion (CTE) the diffractometer is constructed by a single material. Different materials are used for the x-ray window and the bearing balls. The bearing balls will not give problems because differences in expansion are set off by the spring bush. The stresses arising in the x-ray window are calculated in Appendix F. This stress does not exceed the maximum material stresses but the bond between the window and the box still has to be investigated.

The stability of the source/detector position depends on temperature changes in the structure. During diffractometer operation the temperature will be kept within a temperature range of 1° Celsius. Uniform heating of the complete diffractometer has no influence on the diffractometer performance since no difference in expansion will appear in the levers. An equal extension of the levers will not give differences in the diffraction results. Temperature changes in the diffractometer construction appear by power input of the piezo's and the encoders. The total dissipated heat of the piezo's and angle encoder is calculated in Appendix F:

piezo's	: 0.47 W,
angle encoder	: 1.5 W.

Within the diffractometer structure the dissipated heat is:

piezo's	: 14 mW,
angle encoder	: 165 mW.

The power dissipation of the angle encoder is relatively high due to a high read-out frequency (225kHz). For the diffractometer a much lower read-out frequency ($\approx$ 200Hz) will be sufficient thus making a lower power dissipation possible.

The dissipated heat of the piezo's is only transported by conduction. Because of the vacuum convection is not existing and heat radiation is negligible at low temperatures and small temperature changes. Because of the relative high conductivity of steel and the low heating power, the heat dissipation of the piezo's is assumed to bring about a uniform heating of the stepper, holder and levers. The resulting increase in temperature and the corresponding elongation of the levers during one diffraction run (90 $^\circ\theta$) are 0.7 ° Celsius and 0.7 μm.

7.3 Space qualification and planetary protection policy

The diffractometer design is based on accelerations of 40g. Stresses are in the construction are kept low. For the main parts the eigenfrequencies are verified with FEM analysis, see Appendix G. The holding force of the clamps is not sufficient to keep the levers in place during launch. Therefore a launch-lock is needed. This launch-lock should also constrain the axial movement of the levers. In order to avoid large thermal stresses the construction is based on a single material. To avoid cold-welding, mating surfaces of moving elements are made of dissimilar materials. The components used in the diffractometer are all vacuum compatible and meet the conditions for space qualification. To meet planetary protection

policy requirements the use of organic materials is avoided. All structural elements are made of metal.

7.4 Specifications

		Requirements	Obtained
Angle resolution	μrad	< 20	< 15
Angle range (2θ)		$4 - 160^\circ$	$0 - 170^\circ$
Tolerance Δr	μm	20	1
Tolerance Δz	μm	500	1.5
Tolerance r_r	μrad	75	90
Tolerance $r_{\theta-source}$	μrad	200	45
Tolerance $r_{\theta-detector}$	μrad	1000	90
Tolerance $r_{z-source}$	μrad	7.5	5
Tolerance $r_{z-detector}$	μrad	100	10
Volume (LxWxH)	mm	220x60x120	240x73x152
Mass	kg	0.8	0.45
Power	W	2	2

Table 7.1: Diffractometer specifications

In table 7.1 the required and obtained diffractometer specifications are compared. The obtained specifications meet almost completely the requirements.

The rotation around the r-axis can be larger than the allowed rotation. Rotation around this axis causes peak broadening in the diffraction plot. The exact influence and consequences should be investigated.

The diffractometer dimensions do not meet the requirements. This is because a diffractometer radius of 100 mm is chosen. A smaller diffractometer circle is possible, to about half the current size, but the influence of finite source size should be investigated. The width of the box is partly determined by the 'width' of the detector, currently about 30 mm. A decrease in detector 'width' would decrease the width of the box.

It should be noted that the mass mentioned is only the mass of the basic components. Extra mass will be added due to wiring, control and data processing units.

Chapter 8

Conclusions and recommendations

In the preceding chapters the design of the diffractometer is presented. This chapter presents the conclusions made and the recommendations for future work.

8.1 Conclusions

A design is made of a diffractometer for use on a Mars-rover. The diffractometer requirements included a target dimension of 220x60x120 mm, a target mass of 0.8 kg and a maximal power consumption of 2 Watt. It should meet the requirements for space qualification and planetary protection policy. Furthermore it should meet the geometrical tolerances, needed for an accurate diffraction plot. The source and detector had to be positioned with an angle resolution better than 20 μrad over an angle range of 2-80°(θ) with respect to the specimen surface.

The designed diffractometer contains a radioactive source and a solid state detector. These are moved along a guide by means of a piezo stepper. The piezo-stepper provides a high angle resolution in combination with lever fixation when idle. Compact holders of the piezo steppers and the source/detector enable a large angle range. For guiding the motion, two lightweight levers rotate in a hybrid, integrated bearing setup. By means of a single harmonica bush, the bearing sets of both levers are preloaded. This setup provides high accuracy in combination with a low mass and volume. An optical encoder provides the angle information of the levers. The read-heads are mounted on the bearing housing. In this way the cables will not disturb the lever motion and the heat production will not disturb the position accuracy of the source/detector. The diffractometer components are enclosed by two shells, providing stiffness, vacuum environment and protection. An X-ray window provides passage for the X-rays. All parts are made of one type of steel except for the X-ray window and the bearing balls. In this way high thermal stresses during spaceflight can be avoided. For mass and part reduction the shells are welded to the baseplate. The power consumption of the piezo steppers is very low and does not have major influence on position accuracy.

The diffractometer almost completely meets the requirements. The diffractometer has a very low mass of 0.45 kg (excluded electronics) and a power consumption of 2 Watt. An even lower power consumption is possible when the read-out frequency of the angle encoder is decreased. The dimensional requirements are not completely met. The actual size is 240x73x152 mm.

This is partly because of the choice of a diffractometer circle of 100 mm. Reducing this radius to about half the actual length is possible. The components used, all meet the conditions for space qualification and comply as much as possible to the planetary protection policy.
The geometrical tolerances are met except for the rotation around the r-axis (90 μrad obtained, 75 μrad required). The influence of this deviation on the diffraction plot has to be investigated. The angle resolution of the diffractometer is 15 μrad and can be further reduced. The angle range for the source and detector is 0-85°(θ).

8.2 Recommendations

The diffractometer contains a radioactive source and a solid state detector. Their volume and mass values are assumed. Exact specifications have to be provided experts. When the specifications are known, the mounting of the two should be reviewed.

Stepper performance is dependent on piezo motion and friction. Tests shall provide information about the actuation force, step behaviour and maximal resolution.

For the X-ray window, welding of beryllium to steel is assumed. Tests should make clear if this is possible.

To increase the accuracy, the rotation of the specimen instead of the source should be considered. Deviations in specimen position will give less errors in the diffraction plot than deviations in the source position. Possibly also mass can be reduced .

The diffractometer radius is taken at 100 mm. This radius can be decreased to about half the size. This would result in mass savings and increased stiffness of the box. The stepper will be able to keep the same angle resolution by making smaller steps. It should be investigated if the diameter of the radioactive line source will not become a problem in the diffraction data.

Paragraph 6.12 gives suggestions for the launch-lock. Applicability and integration of commercially available launch-locks should be examined. The valve mentioned in 6.10 has not been looked at. A valve design has to be made or commercial valves should be considered.

Glue is intended to be used for mounting components. Most glues are not X-ray resistant. Further investigation should make clear if glue can be applied and if alternatives or shielding are necessary.

For commercial application on earth, the design has to be reviewed. For use on earth other requirements will become more important. Costs will play a more important role and mass will be of less importance. The integrated bearing setup can be replaced by a conventional setup with angular ball bearings at the expense of some accuracy, mass and volume. The use of an X-ray source will also imply additional government regulation on radiation safety. Radiation shielding will be necessary. When using an X-ray tube instead of a radioactive source, the levers and stepper should be reviewed. Depending on size, mass and wiring, fixing the source and rotating the specimen should be considered.

Bibliography

[1] ECSS. Space product assurance, ECSS standardisation collection, ECSS-Q-70-71A. www.ECSS.nl, June 2005.

[2] ECSS. Space product assurance, ECSS standardisation collection, ECSS-E-30-3A. www.ECSS.nl, June 2005.

[3] Moxtek. www.moxtek.com, June 2005.

[4] MarkeTech International Inc. www.mkt-intl.com, October 2005.

[5] Goodfellow Corporation. www.goodfellow.com, October 2005.

[6] Physik Instrumente (PI). http://www.physikinstrumente.com, August 2005.

[7] NASA. Space Mechanisms Lessons Learned study. http://www.grc.nasa.gov/WWW/spacemech/vol1.html, August 2005.

[8] R.Delhez et all. Pasteur call for ideas. http://www.spaceflight.esa.int/users/file.cfm?filename=coord-ao-exomars, April 2005.

[9] Farrand Controls. www.inductosyn.com, June 2005.

[10] MicroE Systems. www.microesys.com, June 2005.

[11] ESA. www.esa.int, July 2005.

[12] ESA. http://www.esa.int/SPECIALS/Aurora/index.html, July 2005.

[13] Cospar. http://www.cosparhq.org/scistr/PPPPolicy.htm, July 2005.

[14] TNO instrument workshop. Stieltjesweg 1, 2628 CK Delft. personal communication, June 2005.

[15] GTD Eindhoven Universitiy of Technology. Postbus513 5600 MB, Eindhoven. personal communication, June 2005.

[16] CANBERRA Eurisys Benelux NV/SA. Research Parc, Pontbeeklaan - 57, B-1731 Zellik, Belgium. personal communication, May 2005.

[17] Burleigh. Inchworm. www.burleigh.com, April 2005.

[18] W.Barsingerhorn E. de Haas and J.F. van der Veen. Piëzo elektrische draaitafel. *Mikroniek*, May 1996.

[19] K.J. Schard. Geintegreerde lagereenheden. *Mikroniek*, February 1989.

[20] B.D. Cullity and S.R. Stock. *Elements of X-ray diffraction.* Prentice-Hall, 2001.

[21] G.F. Knoll. *Radiation detection and measurement.* John Wiley & Sons, New York, 1999.

[22] P.C.J.N. Rosielle and E.A.G. Reker. *Constructieprincipes 1, lecturenote 4007 TUE (in dutch).* Eindhoven University of Technology, 2002.

[23] P.Sarrazin et al. Field deployment of a portable X-ray diffraction/X-ray fluorescence instrument on Mars analog terrain. *Powder Diffraction*, Vol.20 128-133, june 2005.

[24] P.C. Breedveld P.J. Feenstra. Analysis of a surface acoustic wave motor. *Ultrasonics, IEEE symposium on*, Vol.2 1133-1136, October 2003.

[25] K. Kurosawa T. Shigematsu and K Asai. Nanometer stepping drives of surface acoustic wave motor. *IEEE transactions on ultrasonics, ferroelectrics and frequency control*, Vol.50 376-385, April 2003.

[26] M.K. Kurosawa T. Shigematsu and K. Asai. Evaluation of surface acoustic wave stepping motion. *Ultrasonics, IEEE symposium on*, Vol.1 637-640, 2001.

[27] S. Brückl. Feed-drive system with a permanent magnet linear motor for ultra precision machine tools. *IEEE international conference on power electronics and drive systems*, Vol.2 821-826, July 1999.

[28] V. Mizariene V.Snitka and V. Baranauskas. Nanometric resolution ultrasonic stepper motor. *Ultrasonics, IEEE symposium on*, Vol.1 553-556, November 1994.

[29] S.D.Lewis and M. Humphries. Space mechanism development lessons to be learned - an independent view. *Proceedings of the 9th European Space Mechanisms and Tribology Symposium*, September 2001.

[30] A. Harnoy. *Bearing Design in Machinery, Engineering Tribology and lubrication.* Marcel Dekker, Inc., 2003. chapter 13.21.3.1, Fatique life of Hybrid Bearings.

[31] W.Beitz and K.H.Grote. *Dubbel, Taschenbuch für den Machinenbau.* Springer Verlag, 1997. p.E98.

[32] K.L. Johnson. *Contact Mechanics.* Cambridge University Press, 1985.

[33] AEA Technology. *Space Tribology Handbook.* AEA Technology plc, 3rd edition, 2002.

[34] R.P. Reed and A.F. Clark. *Materials at low temperatures.* American Society for Metals, 1983.

[35] A. van Beek. *Machine lifetime performance and reliability.* TU Delft, 2004.

[36] Gebrüder Reinfurt GmbH & Co.KG (GRW). *Small, miniature and instrument ball bearings. Technical information*, 2005.

[37] Myonic GmbH. *Standardkatalog*, 2005.

[38] NTN. *NTN Ball and Roller Bearings*, 2005.

[39] Physik Instrumente (PI). *Technical information*, 2005.

[40] R.A.Veugen. Design of a guiding mechanism with flexures for a darwin optical delay line. Master's thesis, Eindhoven Universitiy of Technology, October 2003.

[41] D.M.H.Philips. Een precisie-rotatietafel in zijn vlak gelagerd en aangedreven door piëzo translators. Master's thesis, Eindhoven Universitiy of Technology, June 1994.

Appendix A

Space Qualification

Space qualification involves many issues. Issues concerning:

- lifetime and failure-risk
- maintenance
- vibrations and launch/touch down impact
- vacuum operation

Lifetime and failure risk

Lifetime and failure-risk are directly related to uncertainties in several elements of the design. The 'European Cooperation for Space Standardization'(ECSS) provides safety factors concerning permissible stress levels, uncertainty factors for actuation loads and safety factors concerning lifetime. These factors are shown in table A.1 to A.3.

stress component of concern	Factor
Yield stress	1.1
Ultimate stress	1.2
Fatigue	1.5

Table A.1: Safety factors for stresses (ECSS-E-30 3A [2])

	Factor
Inertia	1.1
Spring	1.2
Friction	1.5
Hysteresis	1.5

Table A.2: Minimum uncertainty factors for actuation loads (ECSS-E-30 3A [2])

Number of predicted cyclic movements	Factor
1000 - 100.000	1.1
> 100.000	1.2

Table A.3: Life test duration factor for in-orbit items (ECSS-E-30 3A [2])

Maintenance

All elements have to be maintenance free since maintenance in space or on Mars is not possible.

Vibrations, launch/touch down impact

Instruments have to survive heavy dynamic loads during launch and touchdown. The load during launch can be expressed as 'Acceleration Spectral Density'(ASD)(g^2/Hz), in terms of the frequency (Hz). The accelerations experienced during launch are approximated by equation A.1 (Mile's equation).

$$G_{rms} = \sqrt{\frac{\pi}{4\xi} f_e(ASD)} \tag{A.1}$$

This equation represents the acceleration for a one dimensional mass-spring-damper system. G_{rms} is the acceleration experienced at an eigenfrequency f_e and is expressed in terms of earth-acceleration (g $\approx 9.81\ m/s^2$). ξ is a damping factor. G_{rms} depends on many factors but in practice it does not exceed 40g. Calculations will be based on this acceleration level. Touch down impact also depends on several factors but is expected not to exceed the launch loads.

Vacuum operation

Space is a high vacuum environment. Vacuum confines the choice of materials used and on the design of components. Main concern is the appropriate choice of materials in relation to outgassing, which may cause change of properties and contamination, and cold-weld which can occur when similar materials are used on mating surfaces.

Appendix B

Diffraction requirements

B.1 Minimal source/detector angle

Clay minerals investigated with XRD using CuKα radiation ($\lambda = 1.542$Å) show important features from a diffraction angle $2\theta = 4°$ upwards. Therefore with a Fe-source, $\lambda = 2.101$Å, the diffraction angle range should start at about $5°2\theta$. The minimal diffraction angle is set at $4°$ 2θ. This implies a minimal source and detector angle of $2°$.

B.2 Resolution

The resolving power of a diffractometer is defined as $\frac{d}{\Delta d}$ and depends on the angle θ and the angle resolution $\Delta\theta$ (equation 5.2):

$$\frac{d}{\mathrm{d}d} = \frac{-1}{\mathrm{d}\theta} \tan\theta$$

Initially a resolving power of 100 is assumed. This means that a plane spacing d can be measured with an accuracy of 1%. When a resolution of 0.001 degree is assumed this resolving power is obtained from about 6 degrees upward.

B.3 Tolerances

Deviations in the source and detector position introduce errors like line broadening and line shift in the diffraction pattern. The exact requirements for the diffraction pattern have to be determined yet. Therefore the requirements in source and detector position are based on a focus space. Where necessary, the requirements following from this approach are divided by two for the source and detector.

An ideal source position is assumed parallel to the z-axis of the diffractometer on a radius r and an angle θ. When an ideal focussing action is assumed a comparison can be made with an ideal lens. Figure B.1 shows a beam of converging rays having a focus point at s. When all the rays of the beam diffracted by the specimen have to be captured within a distance p equal the stepsize, the detector is allowed to move over a distance Δr in beam direction:

$$\Delta r = \frac{\frac{1}{2}p}{\tan\frac{1}{2}\beta}$$

With $\beta = 1°$: $\Delta r = 86\mu m$.

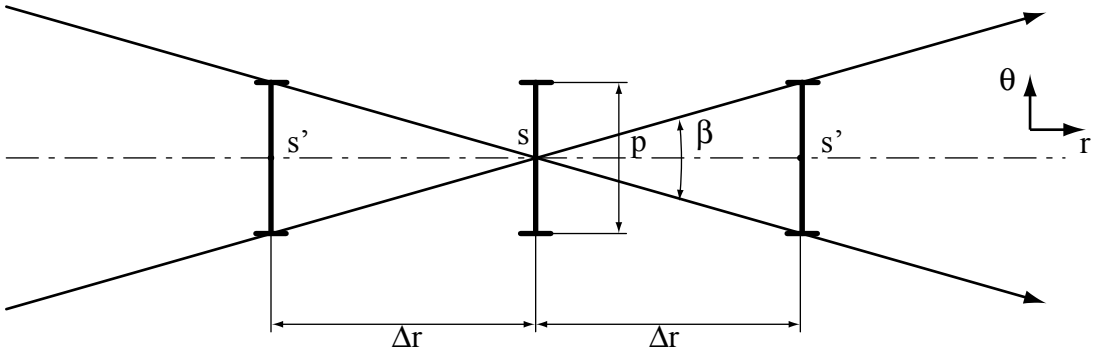

Figure B.1: focus-tolerance

The focus point in figure B.1 is extended to a line focus in z-direction in the diffractometer. When extended in z- and θ-direction, a box can be drawn around the line focus (figure B.2). Deviations falling within this box will not result in loss of rays. The r-z and θ-z planes are considered independently. The z length, the assumed 'width'of the detector, is 20mm. The θ length p equals the stepsize: 1.5 μm.

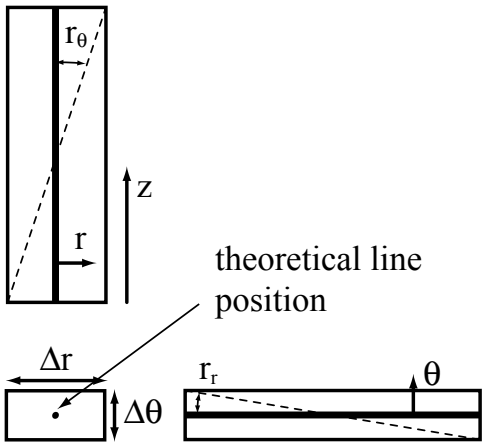

Figure B.2: tolerance space

When considering the r-z plane:
Of the tolerance $2\Delta r = 86mm$, one halve of the tolerance is taken for rotation and the other halve for translation. For the rotation of the source, a z-deviation of the rays on the detector side of 1mm is allowed. This results in:

$$\begin{aligned} \Delta r &= +/-20\mu m \\ r_{\theta-detector} &= 1mrad \\ r_{\theta-source} &= 200\mu rad \end{aligned}$$

When considering the θ-z plane:
Only rotation is of importance, translation along the circumference of the diffractometer circle will be measured directly and has no major influence on the diffraction data. Since the detector 'width' is two times the source length translation in z-direction is not of major importance:

$$\begin{aligned} \Delta z &= +/-0.5mm \\ r_r &= 75\mu rad \end{aligned}$$

When considering the r-θ plane:
Rotation r_z of the detector has no major influence. The rotation r_z of the source is determined by dividing the pitch by two times the radius. The rotation of the detector is less important:

$$\begin{aligned} r_{z-detector} &= 0.1mrad \\ r_{z-source} &= 7.5\mu rad \end{aligned}$$

The tolerances for source and detector are listed in table B.1.

Tolerance +/-		source	detector
Δr	μm	20	20
Δz	mm	0.5	0.5
r_r	μrad	75	75
r_θ	mrad	0.2	1
r_z	μrad	7.5	100

Table B.1: Geometric tolerances

Appendix C

System Layout

C.1 Minimal angle Seeman-Bohlin geometry

The source dimensions are decisive for the minimal angle (θ) the incident beam of the Seeman-Bohlin geometry can reach. Figure C.1 shows the setting near the specimen.

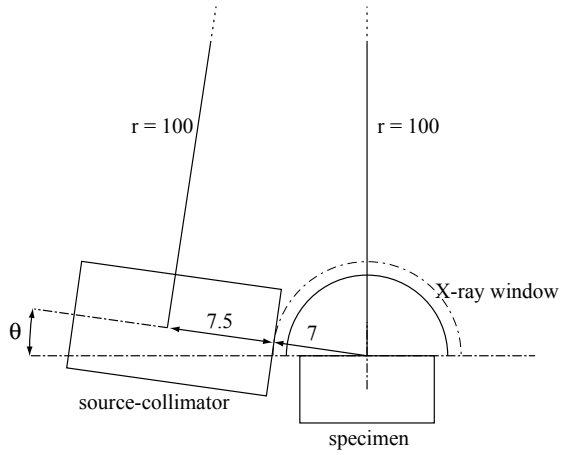

Figure C.1: Minimal angle of the incident beam to the surface for the Seeman-Bohlin geometry

The minimal angle arises from the dimensions of the components. The specimen will have a dimension of 10x10 mm. The X-ray window will enclose the specimen at a distance of 1 mm. The Source is allowed to approach the X-ray window to 1mm.
The final design of the source-collimator is not fixed, the dimension is estimated to be 8x8x15 mm [16]. The collimator is estimated to use halve of the length.
This leads to a total source-specimen (centre) distance of 15 mm.
With these dimensions the approximated minimal angle θ will be:

$$\theta \approx \frac{1}{2} \arctan \frac{15}{100} \approx 4.3^{\circ}(\theta) \tag{C.1}$$

The minimal angle in 2θ will be about 9°.

C.2 Guide accuracy

The accuracy of the carriage position during operation is dependent on the accuracy of the rail and the bearings of the carriage. For calculating the deviations of the guide, the rail is assumed to be straight. Approximation by a straight guide will not give large errors because of a relative large radius in comparison to the wheel base. The guide is examined in the r-θ plane.

The carriage is assumed to have a wheel base of 20 mm and the rail a machining error of three sines on the circumference with a peak to peak error ε of 5 μm. The radius R of the guide is 100mm.

The angle of deviation φ of the rail is approximated by the tangent of the machining error and the peak to peak distance, see figure C.2. This approximation will not give the maximal angle deviation but nevertheless a good estimation.

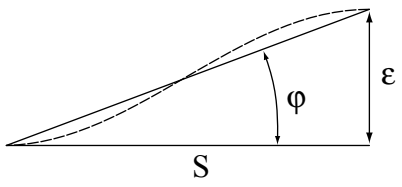

Figure C.2: Approximated angle deviation due to machining errors

The peak to peak distance S on the circumference will be $\frac{1}{6}$ of the circumference: S = $\frac{1}{3}\pi$R. For small angle, $\tan(\varphi) = \varphi$. The angle deviation will be:

$\varphi = \frac{\varepsilon}{S} = 48\ \mu rad$

The angle deviation due to radial run-out of the bearings is calculated in the same way. The radial run-out of high precision bearings is typically 1.5 μm([37],[38], [36]), the wheel base L of the carriage 20mm:

$\varphi = \frac{2\varepsilon}{L} = 150\ \mu rad$

The resulting angle deviation r_z will be 200 μrad.

The radial deviation for the rail and the carriage are 5 μm and 1.5 μm which results in a cumulated error of 6.5 μm.

When the bearings are placed at an angle of 45 degrees relative to the r-θ plane as can be seen in figure 5.4, the errors are $\frac{1}{2}\sqrt{2}$ times the calculated errors: 140 μrad and 3.2 μm.

C.3 Lever accuracy

The accuracy of the lever concept depends on the accuracy of the central bearing. Again a radial run-out of 1.5 μm is taken.

The angle deviation is calculated by dividing the radial run-out of the bearing by the radius of the diffractometer circle:

$r_z = \frac{\varepsilon}{R} = 15\ \mu rad$

The radial deviation will equal the radial run-out of the bearing: 1.5 μm.

When the bearings of the levers are stacked, the maximal error for the stacked lever will be twice the calculated error: 30 μrad and 3 μm.

Appendix D

Bearing

D.1 Static load rating

The static load rating C_0 is defined by ISO 76 (1987) as the static load which would produce a calculated contact pressure at the centre of the most heavily loaded rolling element/raceway contact. For ball bearings this pressure is 4.2 GPa. ISO 76 does not state to which steel this limit applies, but it can be taken to be SAE52100, the most common bearing steel [33]. For AISI 440C a lower max Hertz stress limit of 4GPa is applicable. In accordance with ECSS-E-30-03 a minimum safety factor of 1.25 should be applied against the yield stress. This reduces the allowable stress to 3.4 GPa/3.2GPa for SAE 52100/AISI 440C. For maraging steel 18Ni1700 the same allowable stress is taken as for AISI 440C. Under these conditions the permanent deformation amounts to 1/10,000 of the rolling element diameter.

As a rule of thumb the load of the most heavily loaded ball is given by:

$$F_b = 5P/z \tag{D.1}$$

where P is the bearing load, z the number of ball in the bearing and F_b the load at the most highly loaded ball [35]. For the static load rating this can be rewritten:

$$C_0 = F_1 * z/5 \tag{D.2}$$

where F_1 is the maximum contact load. F_1 for an elliptical contact is defined as:

$$F_1 = (\pi a^* b^* p_c)^3 (\frac{3R'}{E'})^2 \tag{D.3}$$

$$p_c = \frac{p_{max}}{1.5} \tag{D.4}$$

Where p_c is the critical value of the mean contact pressure. R' is the effective radius related to the radius of the individual components, see figure D.1:

$$\frac{1}{R} = \frac{1}{R'_x} + \frac{1}{R'_y} \tag{D.5}$$

$$\frac{1}{R'_x} = \frac{1}{R'_{1,x}} + \frac{1}{R'_{2,x}} \tag{D.6}$$

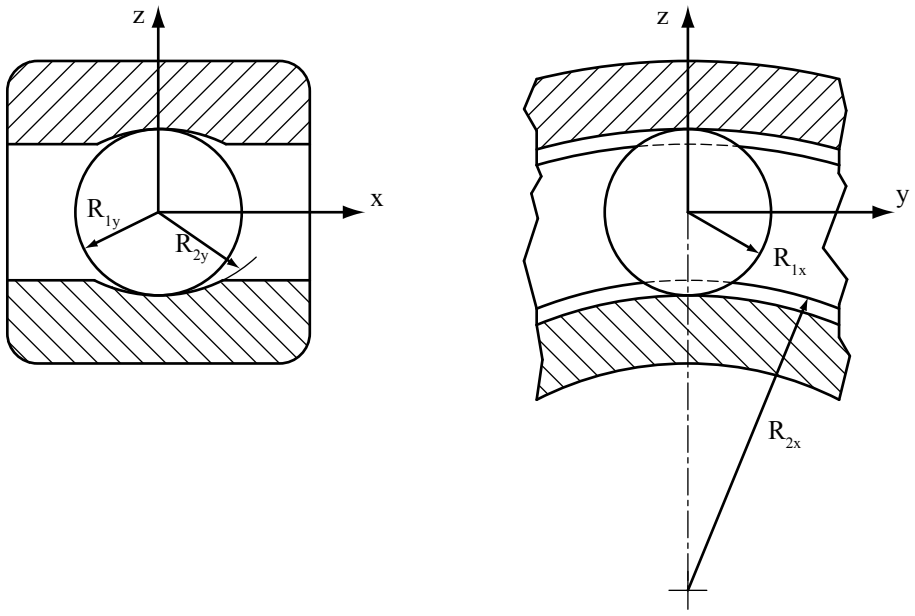

Figure D.1: Curvatures in contact in two orthogonal cross sections of a ball bearing

$$\frac{1}{R'_y} = \frac{1}{R'_{1,y}} + \frac{1}{R'_{2,y}} \tag{D.7}$$

For concave surfaces a negative value for the radius should be substituted.
E′ is the effective modulus of elasticity:

$$\frac{1}{E'} = \frac{1-\nu_1^2}{2E_1} + \frac{1-\nu_2^2}{2E_2} \tag{D.8}$$

a* and b* are the non dimensional semi-axes:

$$a^* = \kappa[1 + \frac{2(1-\kappa^2)}{\pi\kappa^2} - 0.25ln(\kappa)]^{1/3} \tag{D.9}$$

$$b^* = \frac{a^*}{\kappa} \tag{D.10}$$

$$\frac{1}{\kappa} = 1 + (\frac{ln(\frac{16}{\lambda})}{2\lambda})^{1/2} - (ln(4))^{1/2} + 0.16ln(\lambda) \tag{D.11}$$

λ is the ratio of the effective radii $\frac{R'_x}{R'_y}$ or $\frac{R'_y}{R'_x}$, the smallest value of these quotients.

The preceding formulas do not take account of the contact angle of the angular contact ball bearings. However for small angle α there is not significant difference in outcome. With ruby spheres on raceways of maraging steel the static load rating is calculated with the following values:

$r_{1,y}$	$= r_{1,x} = 0.5 d_{ball} = 075$mm	
$r_{2,y}$	$= 0.795$	
$R_{2,x}$	$= 6$mm, $z = 26$	for the inner bearing set
$R_{2,x}$	$= 10.6$mm, $z = 47$	for the outer bearing set
p_{max}	$= 3.2$GPa	
E_{ruby}	$= 350$GPa	([4], [5])
ν_{ruby}	$= 0.22$	
$E_{18Ni1700}$	$= 186$GPa	
$\nu_{18Ni1700}$	$= 0.3$	

Static load rating $C_0 \approx$ will be:
- 243 N for the inner bearing set,
- 514 N for the outer bearing set.

When no plastic deformation is allowed p_c is about equal to the 0.2%-yield strength $R_{p0.2}$. With a $R_{p0.2}$ of 1650 MPa for 18Ni1700 the maximum Hertzian contact load will be:
- 58 N for the inner bearing set,
- 121 N for the outer bearing set.

The number of balls in a bearing is preferably a prime to avoid periodic disturbances. However the levers do not make complete rotations and only at very low speed. Therefore no disturbances due to periodicity are to be expected.

D.2 Spring bush

The calculation of the spring stiffness is based on Fig. 6.24.

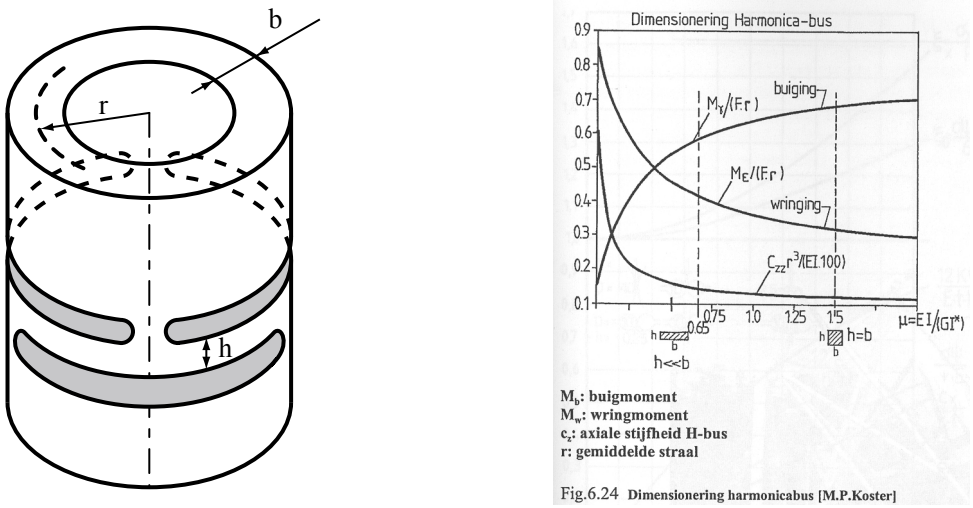

Figure D.2: Dimensioning of a spring bush [22]

Assumed is b=h
From this follows:
$I = h^4/12$ and $\mu = 1.5$

$$c_z = \frac{0.125 * 100EI}{r^3} = \frac{12.5Eh^4}{12r^3} \tag{D.12}$$

for b=h=0.5, r=4.35 mm, E=$2 \cdot 10^{11}$:

$$c_z = \frac{12.5 * 1.86 \cdot 10^{11} * (0.5 \cdot 10^{-3})^4}{12 * (4.35 \cdot 10^{-3})^3} = 1.47 \cdot 10^5 N/m \tag{D.13}$$

For $F_{ax} = 25N \rightarrow u = 0.17mm$

D.3 Solid lubrication

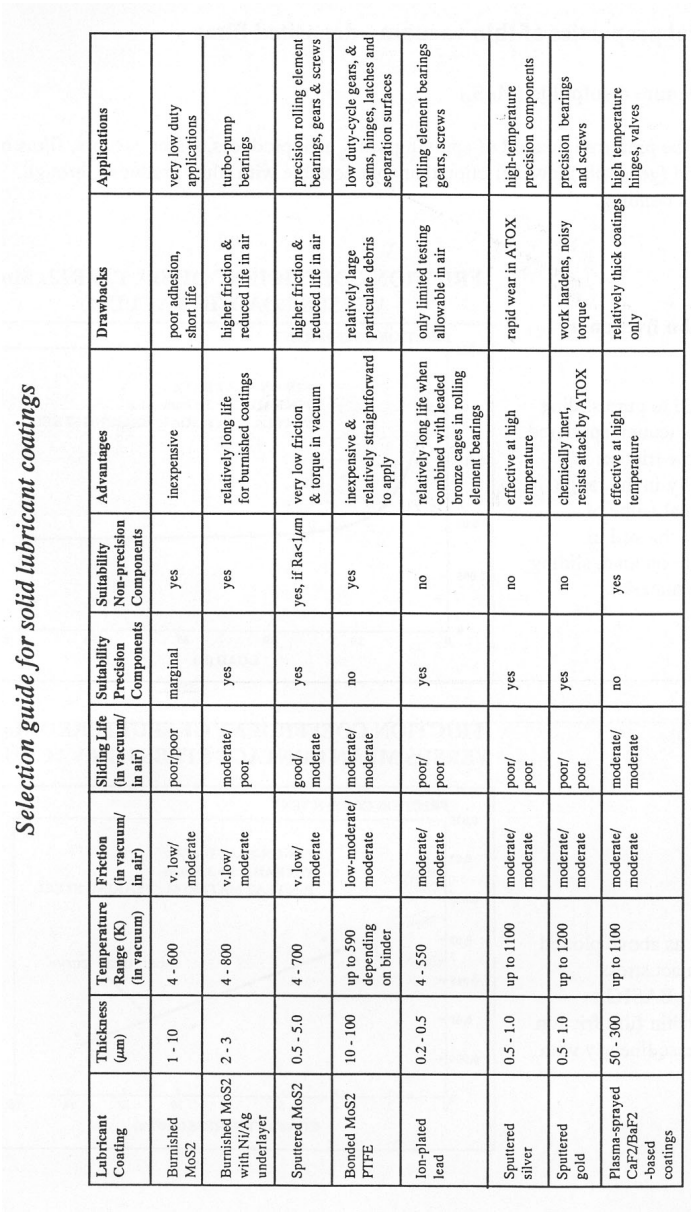

Selection guide for solid lubricant coatings

Lubricant Coating	Thickness (μm)	Temperature Range (K) (in vacuum)	Friction (in vacuum/ in air)	Sliding Life (in vacuum/ in air)	Suitability Precision Components	Suitability Non-precision Components	Advantages	Drawbacks	Applications
Burnished MoS2	1 - 10	4 - 600	v. low/ moderate	poor/poor	marginal	yes	inexpensive	poor adhesion, short life	very low duty applications
Burnished MoS2 with Ni/Ag underlayer	2 - 3	4 - 800	v.low/ moderate	moderate/ poor	yes	yes	relatively long life for burnished coatings	higher friction & reduced life in air	turbo-pump bearings
Sputtered MoS2	0.5 - 5.0	4 - 700	v. low/ moderate	good/ moderate	yes	yes, if Ra<1μm	very low friction & torque in vacuum	higher friction & reduced life in air	precision rolling element bearings, gears & screws
Bonded MoS2 FTFE	10 - 100	up to 590 depending on binder	low-moderate/ moderate	moderate/ moderate	no	yes	inexpensive & relatively straightforward to apply	relatively large particulate debris	low duty-cycle gears, & cams, hinges, latches and separation surfaces
Ion-plated lead	0.2 - 0.5	4 - 550	moderate/ moderate	poor/ poor	yes	no	relatively long life when combined with leaded bronze cages in rolling element bearings	only limited testing allowable in air	rolling element bearings gears, screws
Sputtered silver	0.5 - 1.0	up to 1100	moderate/ moderate	poor/ poor	yes	no	effective at high temperature	rapid wear in ATOX	high-temperature precision components
Sputtered gold	0.5 - 1.0	up to 1200	moderate/ moderate	poor/ poor	yes	no	chemically inert, resists attack by ATOX	work hardens, noisy torque	precision bearings and screws
Plasma-sprayed CaF2/BaF2 -based coatings	50 - 300	up to 1100	moderate/ moderate	moderate/ moderate	no	yes	effective at high temperature	relatively thick coatings only	high temperature hinges, valves

Figure D.3: Selection of solid lubricant coatings [33]

Appendix E

Stepper calculations

E.1 Stroke of the clamp

This subsection calculates the required stroke of the clamp.

Calculated transmission ratio of one lever:
$i_{lever} = 4.5$
$i_{linear-guide} = cos(35) = 0.82$
Total transmission ratio: 0.82*4.5 = 3.7

Actual transmission ratio: $i_{clamp} = 2.9$ (FEM)
The transmission ratio for the clamp is two times the transmission of a single lever:
calculated : 7.4
FEM : 5.8

The total required stroke of the clamp (μm):

surface roughness + thickness variations	5
impression balls (2x) (10N) Appendix G	2
idle stroke	10
total stroke	17

The piezo needs a stroke of 17/(2*2.9)=2.9μm.
The piezo is given an idle stroke of 2 μm to compensate for the tolerance on the shim (1μm)
Total required stroke of the piezo = 5 μm

E.2 Speed profile

X-ray detection takes place when the detector stands still. This is the case when clamp II is fixed. The motion piezo will create a cycloid motion profile:

$$x(t) = (\frac{h_m}{t_m})t - \frac{h_m}{2\pi} sin(\frac{2\pi t}{t_m}) \tag{E.1}$$

$$v(t) = (\frac{h_m}{t_m}) - \frac{h_m}{t_m} cos(\frac{2\pi t}{t_m}) \tag{E.2}$$

$$a(t) = \frac{2\pi h_m}{t_m^2} sin(\frac{2\pi t}{t_m}) \tag{E.3}$$

$$a(t)_{max} = \frac{2\pi h_m}{t_m^2} \tag{E.4}$$

where:
x = displacement [m]
v = velocity [m/s]
a = acceleration [m/s^2]
h_m = stroke [m]
t = time [s]

To keep inertial forces low the maximal piezo acceleration $a(t)_{max}$ is assumed to be 5 m/s^2. The motion time for a piezo stroke h_m is calculated with equation E.4:

Closing the clamp:

$$\left.\begin{array}{ll} h_m & = 3 \cdot 10^{-6}\text{m} \\ a(t)_{max} & = 5\text{m/s}^2 \end{array}\right\} t_{m,c} = 2 \cdot 10^{-3} s$$

Moving the clamp:

$$\left.\begin{array}{ll} h_m & = 1.5 \cdot 10^{-6}\text{m} \\ a(t)_{max} & = 5\text{m/s}^2 \end{array}\right\} t_{m,m} = 1.4 \cdot 10^{-3} s$$

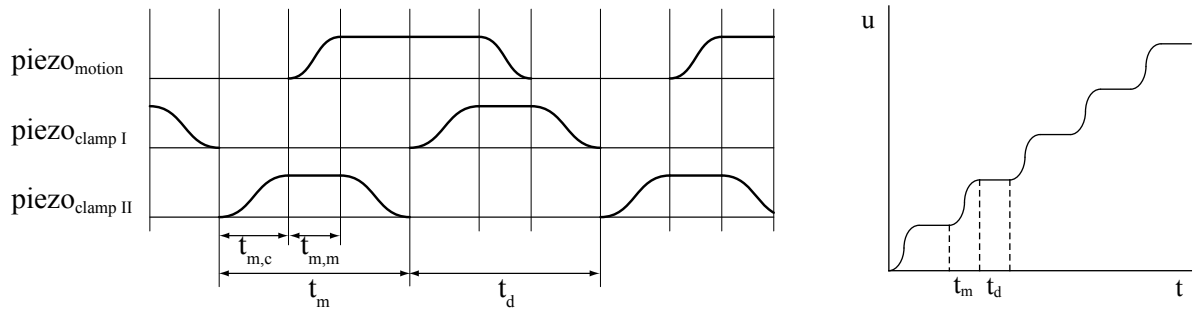

(a) (b)

Figure E.1: (a) Motion profile of the motion and clamp piezo's, (b) motion profile of the stepper

The motion profile of the three piezo's is shown in figure E.1. t_m is the time clamp (I or II) is in motion, t_d the detection time. The total moving time of one clamp is minimal the sum

of 2 times the closing time of the clamp ($t_{m,c}$) and the moving time of the clamp ($t_{m,m}$):

$$t_m = 2t_{m,c} + t_{m,m} \tag{E.5}$$

The detection time is the time the detector stands still, i.e. when $piezo_{clampII}$ is idle. The detection time can be varied but is minimal the motion time of clamp II:

$$t_{d,min} = t_m \tag{E.6}$$

The time it takes to complete one run (90 degree θ) will be:

$$T = \frac{2\pi R}{h_m}(t_m + t_d) \tag{E.7}$$

with R the distance between the clamping points and the axis of rotation of the levers in meter.

When the detection time is chosen to be equal to the moving time the resulting time of one run will be 1150 seconds i.e. about 20 minutes.

E.3 Clamping force

Motion

The maximum acceleration of the piezo (assumed to be on the clamping radius) will be 5 m/s^2. The maximum gravitational acceleration (a_g) on Mars will be 3 m/s^2 (0.3g).
The accelerated mass is assumed to be the complete mass of the clamp and holder: $m = 50 \cdot 10^{-3} kg$.
Assuming the centre of gravity and the clamping point fall together, the maximum acceleration force acting on the clamp will be:
$F = m \cdot a = m \cdot \ddot{h}'(t)_{max} + m \cdot a_g = 50 \cdot 10^{-3} \cdot (5 + 3) = 0.4N$
This force should not exceed the friction force of the clamp:

$$F_f = n \cdot \mu \cdot F_N \tag{E.8}$$

with:

F_f	= friction force [N]
n	= number of friction faces
F_N	= normal force [N]
μ	= coefficient of friction

A μ of 0.15 for Silver/MoS_2 versus silver plated steel is assumed. Figure E.2 gives some alternatives. Further investigation should make clear if other high friction combinations are suitable for space application and if they are in accordance with the planetary protection policy.
In accordance with ECSS-E-30-3 a safety factor of 1.5 for friction has to be applied: μ=0.66*0.15=0.1.

With $n = 2 \rightarrow F_N = \frac{F_N}{n \cdot \mu} = \frac{0.4}{2 \cdot 0.1} = 2N$

This value has to be multiplied by 1.2 according to ECSS-E-30-3: F_N = 2.4 N.

Launch

During launch the clamp should stay in place when subjected to accelerations of 40g. In order to fulfill this requirement the friction force should at least equal the inertial force:
a = 40g = 400 m/s^2
m = 50·10^{-3} kg

F = 20N

This force is distributed over four clamping points.
The normal force on the clamping face needs to be:
$F_N = \frac{F}{n \cdot \mu} = \frac{20}{4 \cdot 0.1} = 50N$

The clamp is not designed to withstand such high forces. Therefore the clamp will need a launchlock in order to stay in place during launch.

The spring used (Gutekunst rz-024yi) will provide a normal force of 4 N. This will create a normal force of 5N on the guide.

Materials	Friction Coefficient		Friction stability in vacuum	Comments	Space Heritage
	Initial	Run-in			
Silver/MoS_2 vs. silver-plated steel	0.25	0.15	Good	This material is designed for slip-ring brushes.	Well-established as slip-ring material. Used as a brake material on SADM of Hubble Space Telescope.
WC/Co	?	?	Good	Tests at Dornier concluded that this was the best brake material of three tested, the others being Al_2O_3/ZrO_2 and Al_2O_3/TiO_2.	Candidate brake material for rotary joints on HERA.
Phenolic/ asbestos	0.5	0.3	Poor	When operated in vacuum the time taken to reach stable friction is unpredictable. Initially friction is high ($\mu = 0.5$) due to moisture retention.	Used on the brakes of the Space Shuttle Remote Manipulator System.
Cr_2O_3	0.2	0.9	Good	Consistently high friction after running-in.	
Al_2O_3/SiC vs Al_2O_3/SiC	In the range 0.55 - 1.5	In the range 0.3 - 0.8	Good	Repeat tests show that although the run-in friction is stable with running time, the magnitude of the friction coefficient differs from run to run.	

Figure E.2: Candidate friction materials and their frictional properties in vacuum [33]

E.4 Hertz contact

The maximum pressure p_{max} and indentation δ can be described by the following formulae:

$$p_{max} = \sqrt[3]{\frac{6FE^2}{\pi^3(1-\nu^2)^2 d^2}} \tag{E.9}$$

$$\delta = \sqrt[3]{\frac{F^2(1-\nu^2)^2}{2E^2 d}} \tag{E.10}$$

for steel-steel ($\nu_1 = \nu_2 = 0.3, E = 1.86e11$):

$$p_{max} = 1.26 \cdot 10^7 \cdot \sqrt[3]{\frac{F}{r^2}} \tag{E.11}$$

$$\delta = 1.82 \cdot 10^{-8} \cdot \sqrt[3]{\frac{F^2}{r}} \tag{E.12}$$

For 18Ni1700:
$p_{max} = 3.2$ GPa (See appendix D, static load rating)

$\frac{F_{max}}{r^2} = 16.4$ MPa

The experienced inertial force during launch F_N will be about 10N. The minimum tip radius of the punch will be:
$r_{min} = \sqrt{\frac{10}{1.27 \cdot 10^7}} = 0.8mm$

When a radius of 1.25 mm is assumed the indentation will be:
$\delta = 0.78\mu m$

A radius of 10 mm will give an indentation of:
$\delta = 0.4\mu m$

E.5 Tangential stiffness ball contact

Johnson [32] gives the formula for the movement of a ball contact on a plane when subjected to a load tangential to that plane:

$$u_t = \frac{\pi(2-\nu)}{4G} F_t \; a \tag{E.13}$$

From this the contact stiffness can be derived:

$$c_{contact} = \frac{F_t}{u_t} = \frac{4G}{\pi(2-\nu)a} \tag{E.14}$$

with

$$a = \left(\frac{3FR}{4E'}\right)^{1/3} \tag{E.15}$$

and

$$G = \frac{E}{2(1+\nu)} \tag{E.16}$$

With a normal force on the punch of 5N, a punch radius of 10mm and steel-steel contact this results in a tangential stiffness of $1.8 \cdot 10^8$N/m. For two clamp points the parallel stiffness will be $3.6 \cdot 10^8$N/m.

E.6 Piezo

The characteristics of the used piezo's are listed in table E.1. The PI P-883.10 is used for releasing the clamps and the PI PL022.30 for movement of the stepper

type	dimensions LxWxH [mm]	Nominal displacement [μm @ 100 V]	Stiffness [N/μm]	Electrical capacitance [nF]	Compressive Tensile limits [N]
PI P-883.10	2x3x9	7	38	210	1000/5
PI PL022.30	2x2x2	2.2	40	25	4000/20

Table E.1: Piezo characteristics [39]

Appendix F

Thermal Considerations

F.1 Stresses at the X-ray window

Due to a deviation in the coefficient of thermal expansion (CTE) of 18Ni1700 and beryllium stresses will appear during spaceflight.
The occurring stress is estimated by the following formula considering a uniform plate held at the edges [34]:

$$\sigma = \frac{E(\alpha_1 - \alpha_2)\Delta T}{(1-\nu)} \tag{F.1}$$

with:

σ	= stress [N/m^2]
α	= coefficient of thermal expansion [μm/m $\cdot$ K]
ΔT	= Temperature change
E	= modulus of elasticity [N/m]
ν	= Poisson′s ratio

This formula is also valid for circular plates [31].
With the following values:

$\alpha_{18Ni1700}$	= 11 μm/m $\cdot$ K
α_{Be}	= 11.5 μm/m $\cdot$ K
ΔT	= 200 K
E_{Be}	= $300 \cdot 10^9$ N/m
ν_{Be}	= 0.18

the estimated stress is 37 MPa. The yield strength of Be and 18Ni1700 are 240 MPa and 1650 MPa. A FEM analysis should give more information on the stresses occurring, especially on the edges.

F.2 Power dissipation

F.2.1 Piezo's

The thermal power, P_{loss}, generated in the piezo during harmonic excitation and the amplifier peak power for sinusoidal operation can be estimated by the following equations [6]:

$$P_{loss} = \frac{\pi}{4} \cdot \tan\delta \cdot f \cdot C \cdot U_{p-p}^2 \tag{F.2}$$

$$P_{max} \approx \pi \cdot C \cdot U_{max} \cdot U_{p-p} \cdot f \tag{F.3}$$

Where:

P_{loss}	= power converted to heat [W]
P_{max}	= amplifier peak power [W]
$\tan\delta$	= dielectric factor
f	= operating frequency [Hz]
C	= actuator capacitance [F]
U_{p-p}	= voltage (peak to peak) [V]
U_{max}	= nominal voltage of the amplifier [V]

Two types of piezo are used. The technical data are listed in table E.1. Assuming a continuous sinusoidal operation and full piezo stroke the power consumption can be calculated:

For clamping:

$\left.\begin{array}{ll} \tan\delta & = 20 \cdot 10^{-3} \\ f_1 & \approx 500 \text{ Hz} \\ C_1 & = 210 \text{ nF} \\ U_{p-p} & = 100 \text{ V} \\ U_{max} & = 50 \text{ V} \end{array}\right\} \begin{array}{lcl} P_{loss} & = & 1.65 \cdot 10^{-2} \text{ W} \\ P_{max} & = & 0.525 \text{ W} \end{array}$

For stepper motion:

$\left.\begin{array}{ll} \tan\delta & = 20 \cdot 10^{-3} \\ f_1 & \approx 700 \text{ Hz} \\ C_1 & = 25 \text{ nF} \\ U_{p-p} & = 100 \text{ V} \\ U_{max} & = 50 \text{ V} \end{array}\right\} \begin{array}{lcl} P_{loss} & = & 2.75 \cdot 10^{-3} \text{ W} \\ P_{max} & = & 8.75 \cdot 10^{-2} \text{ W} \end{array}$

Piezo's only dissipate energy when moving. The clamping piezo is moving about 40 % of the step time when detection time equals moving time. The motion piezo is moving about 25 % of its time. The total dissipation of the three piezo's during step motion will be 14 mW. The dissipation including amplifier power will be 0.47 W. It should be noted that losses in wires are not considered.

Because of the relative high conductivity of steel ($\lambda = 45 W/mK$)and the low heating power the heating of the clamp, holder and levers is assumed to be uniform. The increase in temperature can be calculated with the following formula:

$$\Delta T = \frac{Q}{mc_p} = \frac{PT}{mc_p} \tag{F.4}$$

with:
Q = energy [W]
m = heated mass [kg]
c_p = specific heat capacity [J/kg · K]
P = power converted to heat [W]
T = dissipationtime [s]
ΔT = temperature increase [K]

The values for the clamp and holder and levers are:
m $= 55 \cdot 10^{-3}$ [kg]
c_p = 460 J/kg · K for AISI 440
P = 14 mW
T = 1200 s
The resulting increase in temperature for a 90 degree run will be 0.65 K.

The extension of the levers can be calculated with:

$$\Delta L = L\alpha\Delta T \tag{F.5}$$

The linear coefficient of thermal expansion of 18Ni1700 is 11 μm/mK. The resulting elongation of the levers is 0.72 μm.

F.2.2 Encoder

The angle encoder total power supply will be 5VDC at 300mA. This results in a power dissipation of 1.5 W.

The part the sensor dissipates is 0.16W.

Appendix G

FEM

G.1 Clamp

The calculated transmission ratio, i, of the clamp is 3.7 for one side of the clamp. Due to limited stiffness the actual transmission ratio is smaller. A FEM analysis, see figure G.1 shows a transmission ratio of 2.9.

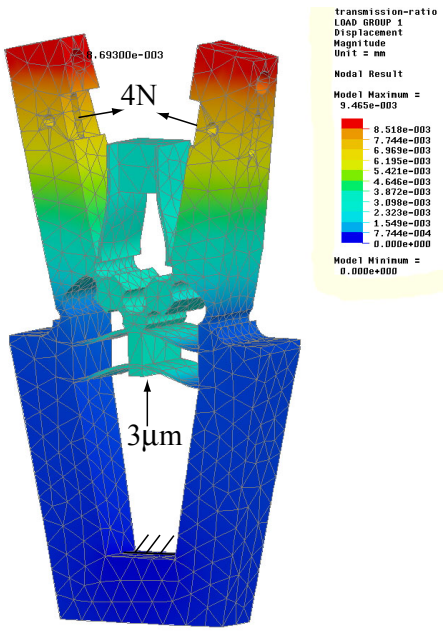

Figure G.1: Transmission ratio of a single side of the clamp: i=$\frac{8.7}{3}$

G.2 Box

Figure G.2 shows the first two eigenfrequencies of the assembled box. The first eigenfrequencies appear at the side plates because of their low stiffness normal to the plane. The box is made of 0.2 mm steel plate. The arrows in the figure show the constrained directions at the edge.

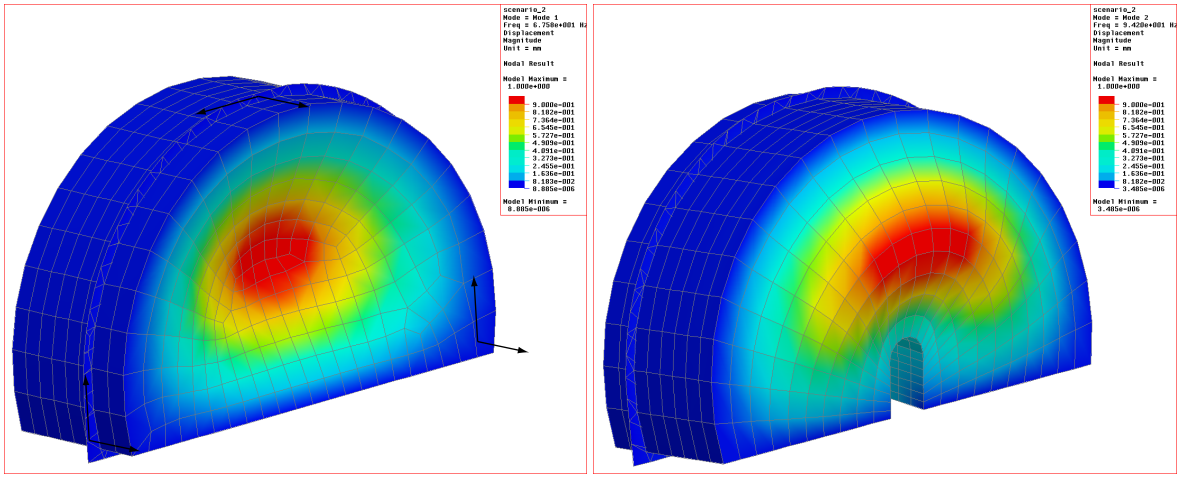

Figure G.2: First two eigenfrequencies of a un-reinforced box: 68Hz, 94Hz

By using stiffeners, the eigenfrequencies are increased with a minimum increase of mass. Figure G.3 shows a reinforced box. The first eigenfrequency is increased from 68 Hz to 321 Hz by adding stiffeners with a total mass of 15g. By using stiffeners care has to be taken with the maximum yield stress. This stress should not be exceeded.

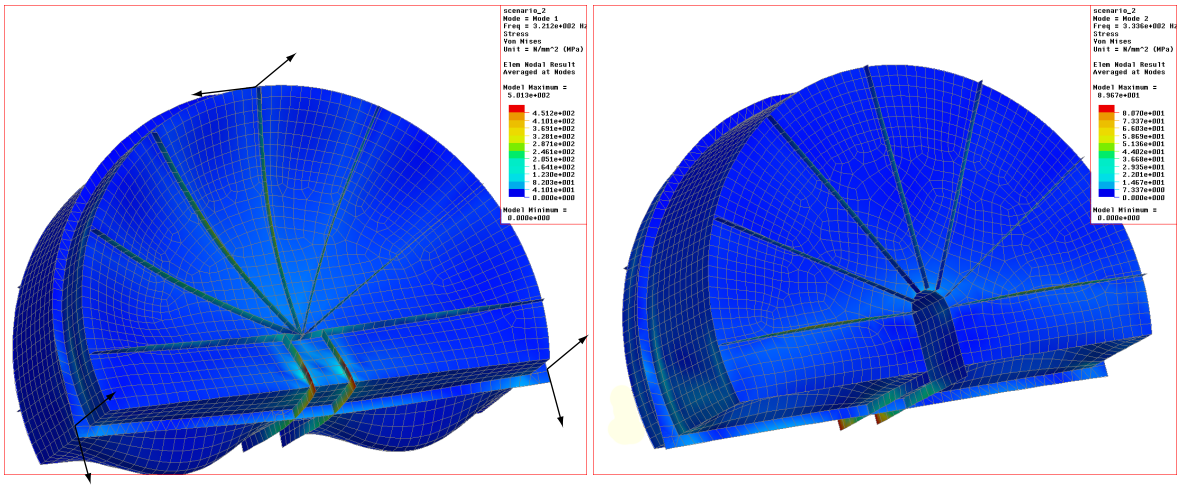

Figure G.3: First two eigenfrequencies of the reinforced box: 321Hz, 334Hz

G.3 Leaf spring bearing setup

Figure G.4 shows the deflection of the leaf spring in the integrated bearing setup due to an axial and radial force of 1N. The calculated axial stiffness is $2.5 \cdot 10^3$ N/m, the radial stiffness $4.3 \cdot 10^6$ N/m.

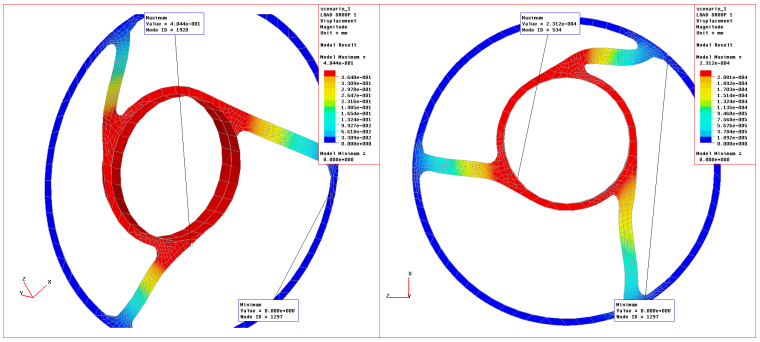

Figure G.4: Axial and radial deflection due to a force of 1N.

G.4 Leaf spring levers

Figure G.5 shows the first eigenmode of one of the leaf springs of the levers. It shows the increase in eigenfrequency from 100 to 250 Hz when the leaf spring is reinforced.

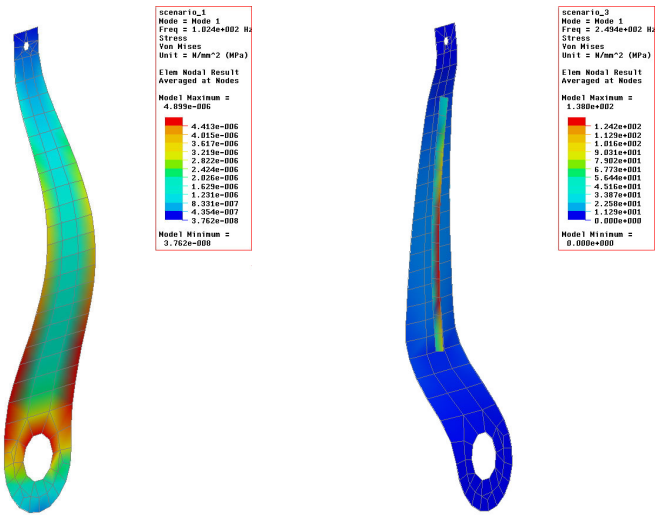

Figure G.5: First eigenfrequency of the leaf spring of the levers.

Appendix H

Angle Encoders

H.1 Inductosyn

Operating principles [9]

Inductive Coupling Between Precision Windings

Precision circuit patterns are etched in copper bonded to the surface of Inductosyn elements. For rotary Inductosyns, the printed circuit pattern comprises hairpin radial turns which repeat on the flat surface of a disk. For linear Inductosyns, the printed circuit pattern comprises parallel hairpin turns which repeat along the surface of a flat bar. The length of one complete cycle of the hairpin patterrn is called the pitch (P). See Figure H.1.

Inductive coupling between windings on a rotary or linear pair of elements is used to measure displacement. The Inductosyn elements are attached to the fixed and moveable machine parts with the elements aligned so that their winding patterns are mutually parallel and separated by a small air gap.

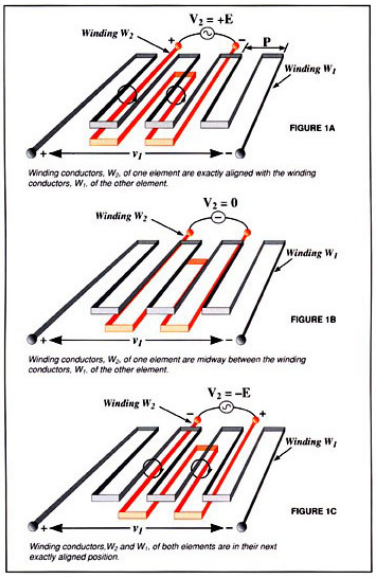

Figure H.1: Inductosyn operation

In Figures 1A, 1B, and 1C, winding W2 moves relative to stationary winding W1. Application of an AC excitation signal, V1, to the winding on one element will cause a current flow in that winding which simultaneously induces a corresponding current flow and output voltage, V2, in the winding of the second element. See Figure 1A. The amplitude and phase of this induced voltage depends on the relative positions of the winding conductors. In Figure 1A, the induced voltage V2 is at maximum amplitude when the winding conductors W2 of one

element are exactly aligned with the winding conductors W1 of the other element. In Figure 1B, the induced voltage, V2, passes through zero when the winding conductors, W2, of one element are midway between the winding conductors, W1, of the other element. The distance moved by W2, from the position shown in Figure 1A to that shown in Figure 1B, is P/4. In Figure 1C, the induced voltage reaches a maximum amplitude of opposite phase when the winding conductors of both elements are in their next exactly aligned position. For simplicity, the phase reversal is shown as a change in polarity in Figure 1C. The signal forms shown in the circles in Figure 1 are indicative of those that would be observed on an oscilloscope connected to the output winding. Winding W2 moved a distance P/2, between the positions shown in Figures 1A and 1C.
Figure H.2 shows an incremental and absolute Inductosyn encoder.

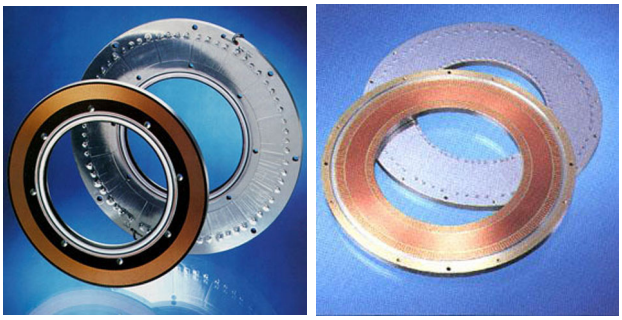

Figure H.2: Incremental and absolute Inductosyn encoder

H.2 Micro-E 3000V

Specifications from MicroE Systems [10]

System Specifications

System

Grating Period	20µm
Signal Period	20µm
System Resolution	5µm - 0.020µm in integer interpolation steps (factory set or user programmed using MicroE SmartSignal Software)
Linear accuracy**	
Interpolation accuracy:	Better than ± 0.12µm over any 20µm movement
Long-travel accuracy:	±1µm accuracy available - consult MicroE Better than ± 3µm for scales up to 130mm Better than ±5µm for scales 155mm to 1m Better than ±5µm per meter for scales 1m or more

**Maximum peak to peak error over the specified movement when compared to a NIST-traceable laser interferometer standard, used at room temperature and with MicroE interpolation electronics.

Rotary Accuracy*	Scale O.D.	Microradians	Arc-Seconds
	12.00mm	±100	±21
	19.05mm	±63	±13
	31.75mm	±38	±7.8
	57.15mm	±19	±3.9
	107.95mm	±10	±2.1

*Based on ideal scale mounting concentricity

Vacuum Encoder System

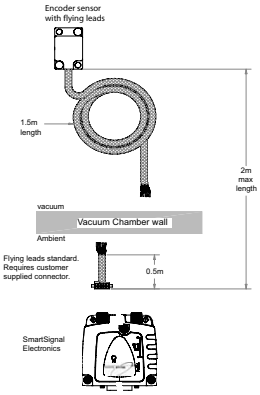

Sensor Size

W:	12.70mm	0.500"
L:	20.57mm	0.810"
H:	8.38mm	0.330"

Operating and Electrical Specifications

Vacuum	10^{-6} Torr, negligible outgassing
Bake Out	Up to 150°C up to 48 hours, non-operating
Power Supply	5VDC ±5% @ 300mA (33mA for sensor)
Temperature	
Operating:	Sensor: 0 to 70°C, SmartSignal electronics 0 to 70°C
Storage:	-20 to 70°C
Humidity:	10 - 90% RH non-condensing
Shock:	1500G 0.5 ms half sine
Sensor Weight:	2.7g (Sensor without cable)
Cable:	The 1.5m vacuum-compatible cable is EMI shielded and comes standard with color coded bare leads for customer termination wit

Mechanical Information - Sensor

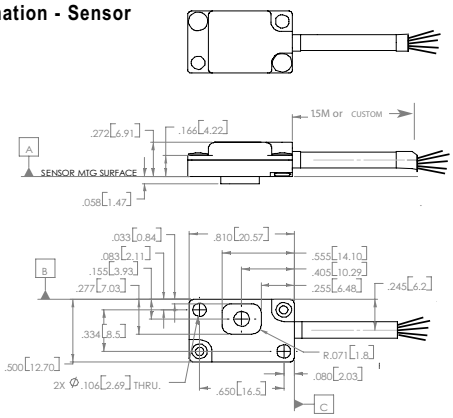

All Specifications are subject to change. All data is accurate to the best of our knowledge. MicroE Systems is not responsible for errors.

Appendix I

TNO Science & Industry

This work is carried out on the authority of the Space Department and at the Precision Mechanics Department of TNO in Delft, the Netherlands.

TNO was established by law in 1932 to support companies and governments with innovative, practicable knowledge. Nowadays TNO holds a prominent position in national and international science and develops new knowledge together with universities, technology top institutes and companies. Five core areas are distinguished in which R&D efforts and expertise are concentrated:

- TNO Quality of Life
- TNO Defence Security and Safety
- TNO Science and Industry
- TNO Environment and Geosciences
- TNO Information and Communication Technology

The Space Department and Precision Mechanics Department are part of TNO Science & Industry, Business Unit Opto Mechanical Instrumentation (OMI) as can be seen in figure I.1.

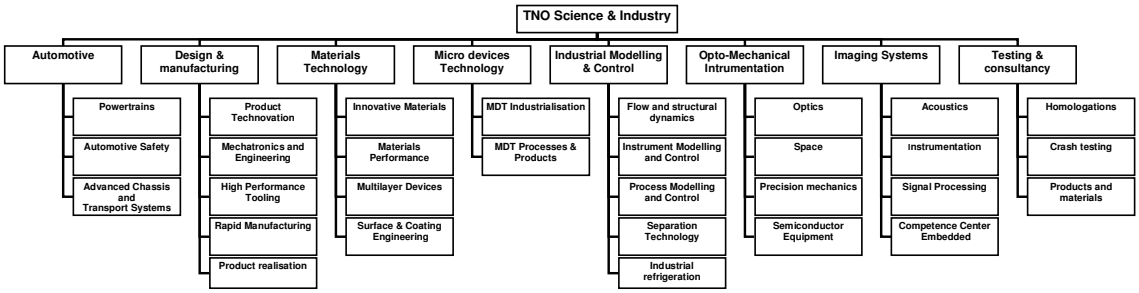

Figure I.1: TNO Science & Industry organisation chart

The Space Department delivers complete instruments and the subsystems for instruments used to observe planet Earth and as part of scientific space projects.

The Precision Mechanics Department develops and supplies the mechanical expertise required in opto-mechanical systems used in space industry and lithographic projects. Products and services include optical confirmations, alignment mechanics, extremely stable constructions, mechanisms of the highest accuracy and microsorting and micromanipulation of microspores.